Electronic supplementary information (ESI)
for
Enhanced luminescence properties through heavy ancillary ligands in [Pt(C^N^C)(L)] complexes, L = $AsPh_3$ and $SbPh_3$

Rose Jordan,[a] Iván Maisuls,[b] Shruthi S. Nair[c,d], Benjamin Dietzek-Ivanšić,*[,c,d] Cristian. A. Strassert*[,b] and Axel Klein*[,a]

[a] University of Cologne, Faculty for Mathematics and Natural Sciences, Department of Chemistry, Institute for Inorganic Chemistry, Greinstrasse 6, D-50939 Köln, Germany.
[b] Westfälische Wilhelms-Universität Münster, Institut für Anorganische und Analytische Chemie, CiMIC, CeNTech, Heisenbergstraße 11, D-48149 Münster, Germany.
[c] Friedrich Schiller University Jena, Institute for Physical Chemistry (IPC), Helmholtzweg 4, 07743 Jena, Germany.
[d] Leibniz Institute for Photonic Technologies Jena (IPHT) Albert-Einstein-Str. 9, 07745 Jena, Germany.

Contents

Supporting Tables

Table S6 Electrochemical data for the ligands H_2dpp and H_2dba and the complexes [Pt(C^N^C)($PnPh_3$)] (Pn = P, As, Sb).
Table S7 UV-vis absorption data of the ligand H_2dpp and the complexes [Pt(dpp)($PnPh_3$)] (Pn = P, As, Sb).
Table S8 UV-vis absorption data of the ligand H_2dba and the complexes [Pt(dba)($PnPh_3$)] (Pn = P, As, Sb).

Experimental Section

Materials. All manipulations were carried out using standard *Schlenk* techniques. The reaction solvent CH_2Cl_2 (HPLC grade) was degassed in three freeze-pump-thaw cycles and dried over activated 4 Å molecular sieves. [Pt(dpp)(dmso)], [Pt(dba)(dmso)], [Pt(dpp)(PPh_3)] and [Pt(dba)(PPh_3)] were prepared following reported procedures.[1,2]

Instrumentation – general. NMR spectra were recorded on a 600 MHz *Bruker* Avance II+ spectrometer or a 500 MHz *Bruker* Avance III spectrometer. All measurements were done at room temperature. ^{1}H signals were referenced to TMS. The following abbreviations are used to indicate the multiplicity of signals: s = singlet, d = doublet, t = triplet, q = quartet, quint = quintet, m = multiplet. The assignment of the signals to the protons present in larger molecules was done with the help of 2D NMR experiments. High resolution electrospray ionisation (HR-ESI) mass spectra were measured on a Thermo Scientific LTQ Orbitrap XL spectrometer using an FTMS analyser. Cyclic voltammetry measurements were performed in a baked-out cyclic voltammetry cell with a glassy carbon working electrode, a platinum counter electrode and an Ag/AgCl pseudo reference electrode. Scans were carried out in 0.1 M nBu$_4$NPF$_6$ THF solution at a scan rate of 50 mV/s or 100 mV/s. The potential was regulated using a *Metrohm* μStat400 potentiostat. The measured data was referenced to the $FeCp_2/FeCp_2^+$ redox pair. UV-vis absorption spectra were measured on a *Varian* 50 Scan UV-vis photometer. Quartz glass cuvettes with a length of 1 cm were used and all spectra were baseline corrected.

Photoluminescence experiments. Photoluminescence spectra at were recorded with a *Spex FluoroMax-3* spectrometer. Luminescence quantum yields were determined with a *Hamamatsu Photonic*s absolute PL quantum yield measurement system (C9920–02), equipped with a L9799-01 CW Xenon light source, monochromator, photonic multichannel analyser and integrating sphere. An error ± 2% for the photoluminescence quantum yield Φ is estimated. Degassed spectroscopic grade solvents were used. Photoluminescence quantum yields were measured with a Hamamatsu Photonics absolute PL quantum yield measurement system (C9920-02) equipped with a L9799-01 CW Xe light source (150 W), a monochromator, a C7473 photonic multi-channel analyser, an integrating sphere and employing U6039-05 software (Hamamatsu Photonics, Ltd., Shizuoka, Japan). Steady-state excitation and emission spectra were recorded on a FluoTime 300 spectrometer from PicoQuant equipped with: a 300 W ozone-free Xe lamp (250-900 nm), a 10 W Xe flash-lamp (250-900 nm, pulse width ca. 1 μs) with repetition rates of 0.1 – 300 Hz, a double-grating excitation monochromator (Czerny-Turner type, grating with 1200 lines/mm, blaze wavelength: 300 nm), diode lasers (pulse width < 80 ps) operated by a computer-controlled laser driver PDL-828 "Sepia II" (repetition rate up to 80 MHz, burst mode for slow and weak decays), two double-grating emission monochromators (Czerny-Turner, selectable gratings blazed at 500 nm with 2.7 nm/mm dispersion and 1200 lines/mm, or blazed at 1200 nm with 5.4 nm/mm dispersion and 600 lines/mm) with adjustable slit width between 25 μm and 7 mm, Glan-Thompson polarizers for excitation (after the Xe-lamps) and emission (after the sample). Different sample holders (Peltier-cooled mounting unit ranging from –15 to 110 °C or an adjustable front-face sample holder), along with two detectors (namely a PMA Hybrid-07 from PicoQuant with transit time spread FWHM < 50 ps, 200 – 850 nm, or a H10330C-45-C3 NIR detector with transit time spread FWHM 0.4 ns, 950-1700 nm from Hamamatsu) were used. Steady-state spectra and photoluminescence lifetimes were recorded in TCSPC mode by a PicoHarp 300 (minimum base resolution 4 ps) or in MCS mode by a TimeHarp 260 (where up to several ms can be traced). Emission and excitation spectra were corrected for source intensity (lamp and grating) by standard correction curves. For samples with lifetimes in the ns order, an instrument

response function calibration (IRF) was performed using a diluted Ludox® dispersion. Lifetime analysis was performed using the commercial EasyTau 2 software (PicoQuant). The quality of the fit was assessed by minimizing the reduced chi squared function ($\chi 2$) and visual inspection of the weighted residuals and their autocorrelation. Assuming unitary intersystem crossing efficiencies (due to the chelation of a late transition metal), the average radiative and radiationless deactivation rate constants (k_r and k_{nr}, respectively) were calculated according to the following equations and relationships:

$$k_r = \frac{\Phi_L}{\tau_L}, \qquad k_{\mathrm{nr}} = \frac{1-\Phi_L}{\tau_L}, \qquad \text{and } \tau_{\mathrm{L}} = \frac{1}{k_r + k_{nr}}$$

where τ_L is the excited state lifetime (or amplitude-weighted average lifetime, $\tau_{av\_amp,}$ for multiexponential decays).

Transient absorption spectroscopy. The ultrafast transient absorption (TA) experiments were performed using a custom-built setup described in detail elsewhere.[3] We employ a Ti-Sapphire (Astrella, Coherent Inc.) regenerative amplifier, which produces 800 nm, 85-fs pulses (laser power-5W, pulse-to-pulse repetition rate of 1 kHz). A part of the amplifier output at 800 nm is directed to an optical parametric amplifier (TOPAS Prime, Light Conversion) to generate the pump at 340 or 500 nm. The excited state dynamics was studied with white-light supercontinuum pulses (generated by focusing a small portion of the amplifier output onto CaF_2 crystal). The fs-TA data was analysed using the KIMOPACK tool.[4] Prior to global lifetime analysis, the data was arrival-time (chirp) corrected. The temporal resolution of the experiment is limited to 300 fs because of strong contributions of coherent artefact signals to the data interfere with reliable analysis of the pump-probe data at short delay times. The power of pump-pulse used was in the range of 0.4 to 0.8 mW, OD of sample at the excitation wavelength was in the range of 0.3 to 0.5.

Structure solution from single crystal X-ray diffraction. scXRD measurements were performed on a *Bruker D8 Venture* diffractometer including a *Bruker Photon 100 CMOS* detector using Ag K_α (λ = 0.56086 Å) or Mo K_α (λ = 0.71073 Å) radiation. The crystal data was collected using APEX4 v2021.10-0 [5]. The structures were solved by dual space methods using SHELXT, and the refinement was carried out with SHELXL employing the full-matrix least-squares methods on $F_O^2 < 2\sigma(F_O^2)$ as implemented in ShelXle [6–8]. The non-hydrogen atoms were refined with anisotropic displacement parameters without any constraints. The hydrogen atoms were included by using appropriate riding models.

Computational details. All DFT calculations were performed using ORCA 5.0.2.[9,10] For all atoms, def2-TZVP basis sets, as well as the corresponding def2-ECPs for Pt and Sb, were used unless stated otherwise.[11] The S_0 and T_1 geometries of all compounds were optimised at the BP86 level of theory, using *Grimme's* D3 dispersion correction and the conductor-like polarisable continuum model (CPCM) parametrised for CH_2Cl_2 as an approximate solvation model.[12–17] The geometry optimisations were followed up with numerical frequency calculations in order to confirm the energetic minimum nature of the optimised structure as indicated by the absence of imaginary modes. On the optimised geometries, single point and TD-DFT calculations were performed using the TPSSh functional, *Grimme's* D3 dispersion correction and CPCM parametrised for CH_2Cl_2.[18] Orbital isosurfaces were extracted from the S_0 single point calculations using the ORCA module orca_plot and plotted with the visualisation software CHEMCRAFT at an isovalue of 0.04.[19] For the TD-DFT calculations of absorption spectra for the S_0 states, 40 roots (transitions) for singlets and triplets each were included for each complex. Broadened spectra were obtained using the orca_mapspc module with 2000 cm^{-1} full width at half maximum band broadening. The TD-DFT calculation output was further evaluated using the software package TheoDORE to analyse relative MLCT, L'MCT, LC, LL'CT, and MC contributions to the emissive T_1 states, using the implemented standard algorithm for molecular partitioning of transition metal complexes employing Openbabel.[20] At the T_1 geometries, spin-orbit (SO) calculations were performed using the Zeroth-Order Regular Approximation (ZORA), the TPSSh functional, SARC-ZORA-TZVP basis sets for Pt and Sb, and the CPCM parametrised for CH_2Cl_2.[21–23]

Syntheses

[Pt(dpp)(AsPh$_3$)] 50.0 mg (0.100 mmol, 1.00 eq.) [Pt(dpp)(dmso)] were dissolved in 3 mL CH_2Cl_2 and 30.6 mg (0.100 mmol, 1.00 eq.) $AsPh_3$ were added. After 10 min, the solvent was removed and the crude product was purified via silica gel column chromatography (eluent: CH_2Cl_2). Yield: 54.1 mg (0.074 mmol, 74%) orange solid. ^{1}H NMR (600 MHz, CD_2Cl_2): δ [ppm] = 7.81–7.75 (m, 6H, H13), 7.66 (t, $^3J_{H,H}$ = 8.0 Hz, 1H, H4), 7.46 (t, $^3J_{H,H}$ = 7.4 Hz, 3H, H14), 7.44–7.38 (m, 8H, H10 and H12), 7.34 (d, $^3J_{H,H}$ = 8.0 Hz, 2H, H3), 6.90 (td, $J_{H,H}$ = 7.4 Hz, 1.3 Hz, 2H, H9), 6.62 (td, $J_{H,H}$ = 7.3 Hz, 1.4 Hz, 2H, H8), 6.48 (dd, $J_{H,H}$ = 7.4 Hz, 0.7 Hz, $^3J_{Pt,H}$ = 25.5 Hz, 2H, H7). ^{13}C NMR (125 MHz, CD_2Cl_2): δ [ppm] = 166.7 (C2), 164.9 (C5), 150.8 (C6), 140.4 (C4), 139.2 (C7), 134.5 (C13), 133.2 (C11), 130.4 (C14), 129.8 (C8), 128.6 (C12), 123.8 (C10), 123.5 (C9), 114.8 (C3). HR-ESI-MS(+): m/z = 730.09913 ([M]$^+$, calc.: m/z = 730.09806).

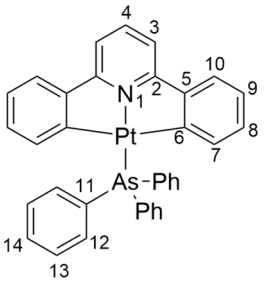

[Pt(dpp)(SbPh$_3$)] 50.0 mg (0.100 mmol, 1.00 eq.) [Pt(dpp)(dmso)] were dissolved in 3 mL CH_2Cl_2 and 38.8 mg (0.110 mmol, 1.10 eq.) SbPh3 were added. After 10 min, the solvent was removed and the crude product was purified via silica gel column chromatography (eluent: CH_2Cl_2). Yield: 50.0 mg (0.064 mmol, 64%) orange solid. ^{1}H NMR (600 MHz, CD_2Cl_2): δ [ppm] = 7.76–7.72 (m, 6H, H13), 7.67 (t, $^3J_{H,H}$ = 8.0 Hz, 1H, H4), 7.50 (m, 3H, H14), 7.45–7.40 (m, 8H, H10 and H12), 7.34 (d, $^3J_{H,H}$ = 8.0 Hz, 2H, H3), 7.03 (dd, $J_{H,H}$ = 7.3 Hz, 1.3 Hz, $^3J_{Pt,H}$ = 32.6 Hz, 2H, H7) 6.93 (td, $J_{H,H}$ = 7.5 Hz, 1.3 Hz, 2H, H9), 6.67 (td, $J_{H,H}$ = 7.3 Hz, 1.3 Hz, 2H, H8). ^{13}C NMR (125 MHz, CD_2Cl_2): δ [ppm] = 166.6 (C2), 164.0 (C5), 150.9 (C6), 141.7 (C7), 140.6 (C4), 136.5 (C13), 130.7 (C8), 130.4 (C14), 129.9 (C11), 129.0 (C12), 124.0 (C10), 123.6 (C9), 115.0 (C3). HR-ESI-MS(+): m/z = 776.08145 ([M]$^+$, calc.: m/z = 776.08028).

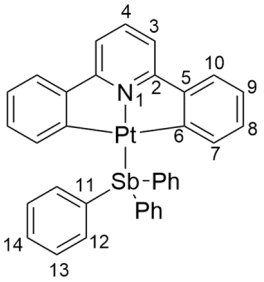

[Pt(dba)(AsPh$_3$)] 35.0 mg (0.068 mmol, 1.00 eq.) [Pt(dba)(dmso)] were dissolved in 3 mL CH_2Cl_2 and 20.7 mg (0.068 mmol, 1.00 eq.) $AsPh_3$ were added. After 40 min, the solvent was removed and the crude product was purified via silica gel column chromatography (eluent: CH_2Cl_2). Yield: 34.3 mg (0.044 mmol, 65%) red solid. ^{1}H NMR (600 MHz, CD_2Cl_2): δ [ppm] = 8.49 (s, 1H, H4), 7.92–7.84 (m, 6H, H15), 7.61 (d, $^3J_{H,H}$ = 8.9 Hz, 2H, H5), 7.56 (d, $^3J_{H,H}$ = 9.1 Hz, 2H, H6), 7.53–7.47 (m, 3H, H16), 7.47–7.42 (m, 6H, H14), 7.37 (dd, $J_{H,H}$ = 7.9 Hz, 0.9 Hz, 2H, H12), 7.06–7.00 (m, 2H, H11), 6.53 (dd, $J_{H,H}$ = 7.1 Hz, 0.7 Hz, $^3J_{Pt,H}$ = 12.7 Hz, 2H, H10). ^{13}C NMR (125 MHz, CD_2Cl_2): δ [ppm] = 162.5 (C8), 155.6 (C2), 147.4 (C9), 135.7 (C10), 135.2 (C15), 134.6 (C4), 134.4 (C7), 133.2 (C11), 130.6 (C16), 130.5 (C13), 129.0 (C14), 128.7 (C5), 124.4 (C3), 122.9 (C6), 121.4 (C12). HR-ESI-MS(+): m/z = 778.09874 ([M]$^+$, calc.: m/z = 778.09806).

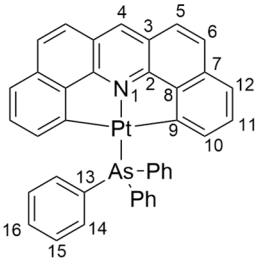

[Pt(dba)(SbPh$_3$)] 31.0 mg (0.060 mmol, 1.00 eq.) [Pt(dba)(dmso)] were dissolved in 3 mL CH_2Cl_2 and 21.1 mg (0.060 mmol, 1.00 eq.) $SbPh_3$ were added. After 45 min, the solvent was removed and the crude product was purified via silica gel column chromatography (eluent: CH_2Cl_2). Yield: 41.7 mg (0.051 mmol, 84%) red solid. ^{1}H NMR (600 MHz, CD_2Cl_2): δ [ppm] = 8.51 (s, 1H, H4), 7.86–7.80 (m, 6H, H15), 7.63 (d, $^3J_{H,H}$ = 8.9 Hz, 2H, H5), 7.58 (d, $^3J_{H,H}$ = 8.9 Hz, 2H, H6), 7.54–7.49 (m, 3H, H16), 7.48–7.43 (m, 6H, H14), 7.40 (dd, $J_{H,H}$ = 6.2 Hz, 4.2 Hz, $^5J_{Pt,H}$ = 15.4 Hz, 2H, H12), 7.12–7.05 (m, 4H, H10 and H11). ^{13}C NMR (125 MHz, CD_2Cl_2): δ [ppm] = 161.3 (C8), 155.5 (C2), 147.5 (C9), 137.9 (C10), 136.5 (C15), 135.4 (C4), 134.8 (C7), 131.3 (C11), 130.5 (C16), 129.8 (C13), 129.2 (C14), 129.0 (C5), 124.6 (C3), 123.0 (C6), 121.6 (C12). HR-ESI-MS(+): m/z = 824.08130 ([M]+, calc.: m/z = 824.08028).

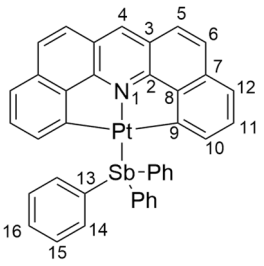

Attempted synthesis of [Pt(dpp)(BiPh$_3$)]

Time resolved NMR study. For *in situ* observation of the reaction of [Pt(dpp)(dmso)] with $BiPh_3$, the latter (0.75 eq.) was added to a solution of the Pt complex in CD_2Cl_2, and the sample was quickly transferred into a 600 MHz NMR spectrometer (see above for details on instrumentation). During the

first few minutes, ^{1}H NMR spectra were recorded in quick succession, but no change was detected between them. ^{1}H NMR (600 MHz, CD_2Cl_2): δ [ppm] = 7.68 (d, $H_{complex}$), 7.65 (d, H_{BiPh3}), 7.53 (t, $H_{complex}$), 7.38 (dd, $H_{complex}$), 7.29 (t, H_{BiPh3}), 7.23 (m, H_{BiPh3}), 7.16 (td, $H_{complex}$), 7.01 (td, $H_{complex}$). For the following 12 h, spectra were recorded every 10 min. The integrals of the observed signals were normalised to a value of 2.00 for the signal at 7.38 ppm which belongs to [Pt(dpp)(dmso)]. The integral of the well-isolated multiplet at 7.29 ppm belonging to $BiPh_3$ decreased significantly over the timescale of the experiment from ca. 4.5 to ca. 3.8 (Fig. S21). The less well-isolated $BiPh_3$ signals decreased in an approximately proportional manner.

MS analysis. A mixture of [Pt(dpp)(dmso)] (68.6 mg, 0.137 mmol, 1.0 eq.) and $BiPh_3$ (120.2 mg, 0.273 mmol, 2.0 eq.) in 4 mL CH_2Cl_2 was stirred at room temperature for 6 d. Precipitation of black solids was observed. The solids were removed by filtration and the filtrate was evaporated to dryness. EI-MS analysis of the residue detected a variety of fragments and coupling products, i.e. phenylated H_2dpp derivatives, derived from the starting materials. m/z = 154.07748 ($[PhPy]^+$, calc.: 154.065674), 208.97958 ($[Bi]^+$, calc.: 208.980399), 230.09628 ($[Hdpp]^+$, calc.: 230.096974), 286.01876 ($[PhBi]^+$, calc.: 286.019524), 306.12744 ($[Hdpp–Ph]^+$, calc.: 306.128275), 382.15869 ($[Ph\text{-}dpp\text{-}Ph]^+$, calc.: 382.159575), 458.19002 ($[Ph_2–dpp–Ph]^+$, calc.: 458.190875), 535.21646 ($[Ph_2–dpp–Ph_2]^+$, calc.: 535.230000).

Supporting Figures

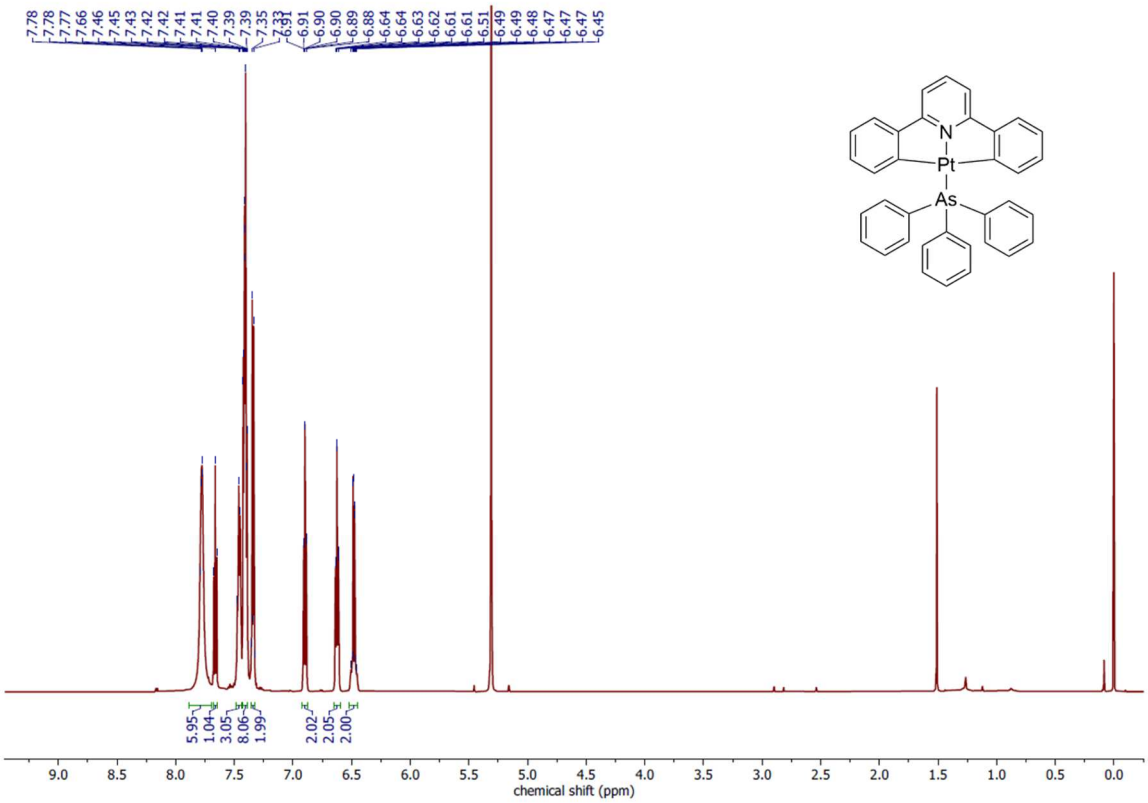

Fig. S1 600 MHz ^{1}H NMR of [Pt(dpp)($AsPh_3$)] in CD_2Cl_2.

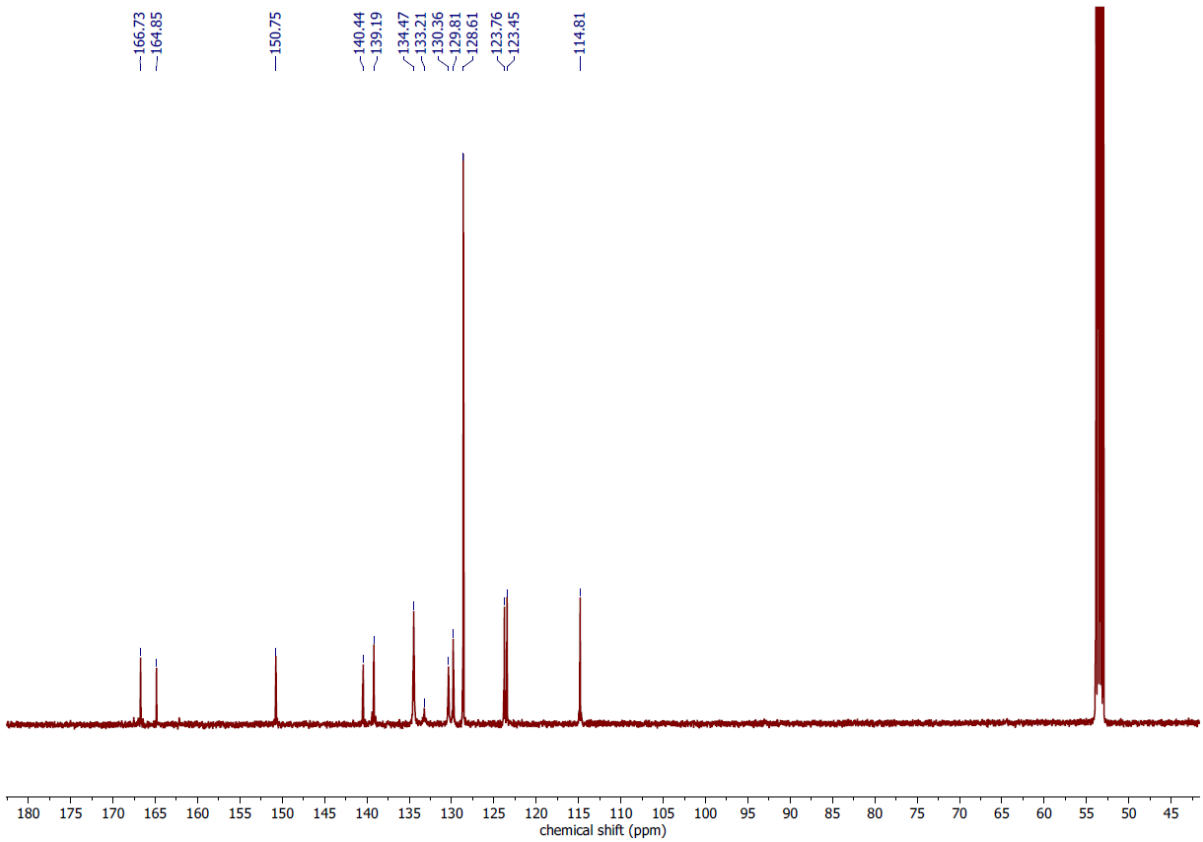

Fig. S2 125 MHz ^{13}C NMR of [Pt(dpp)($AsPh_3$)] in CD_2Cl_2.

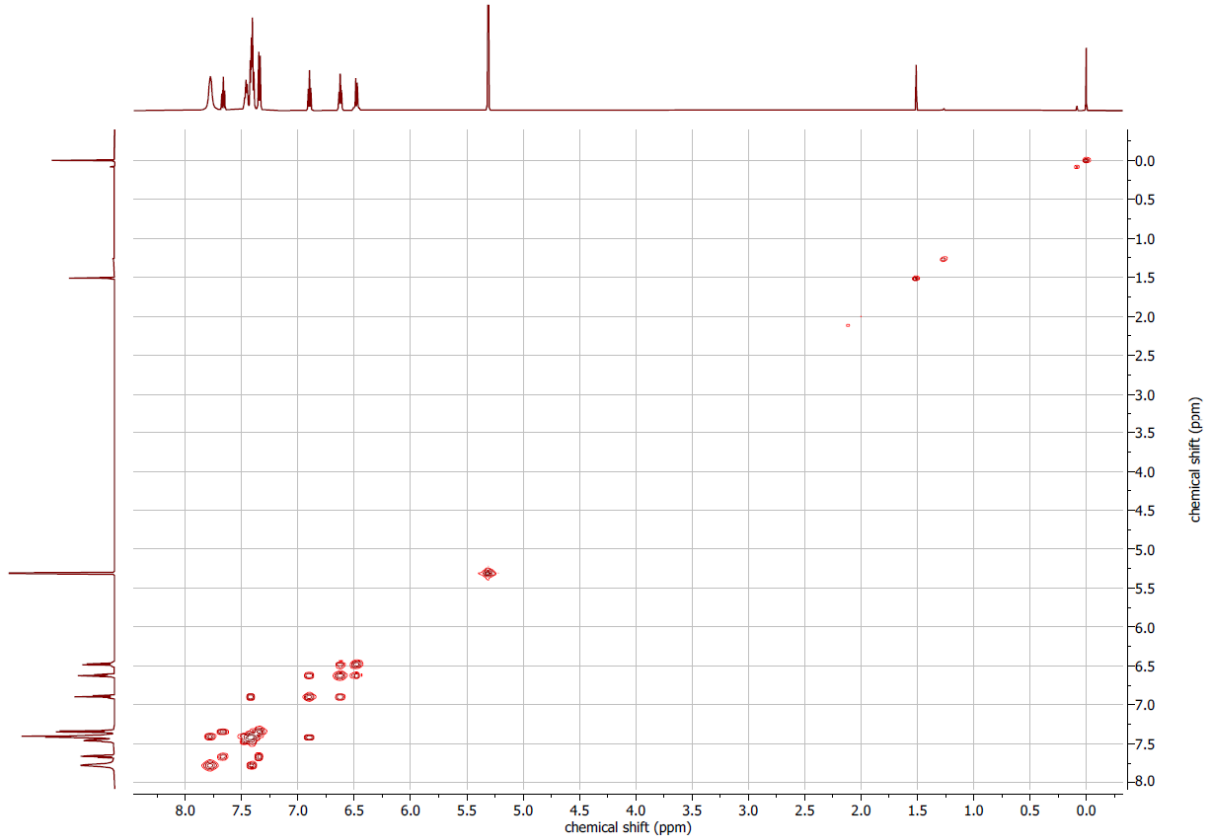

Fig. S3 500 MHz $^{1}H,^{1}H$ COSY of [Pt(dpp)($AsPh_3$)] in CD_2Cl_2.

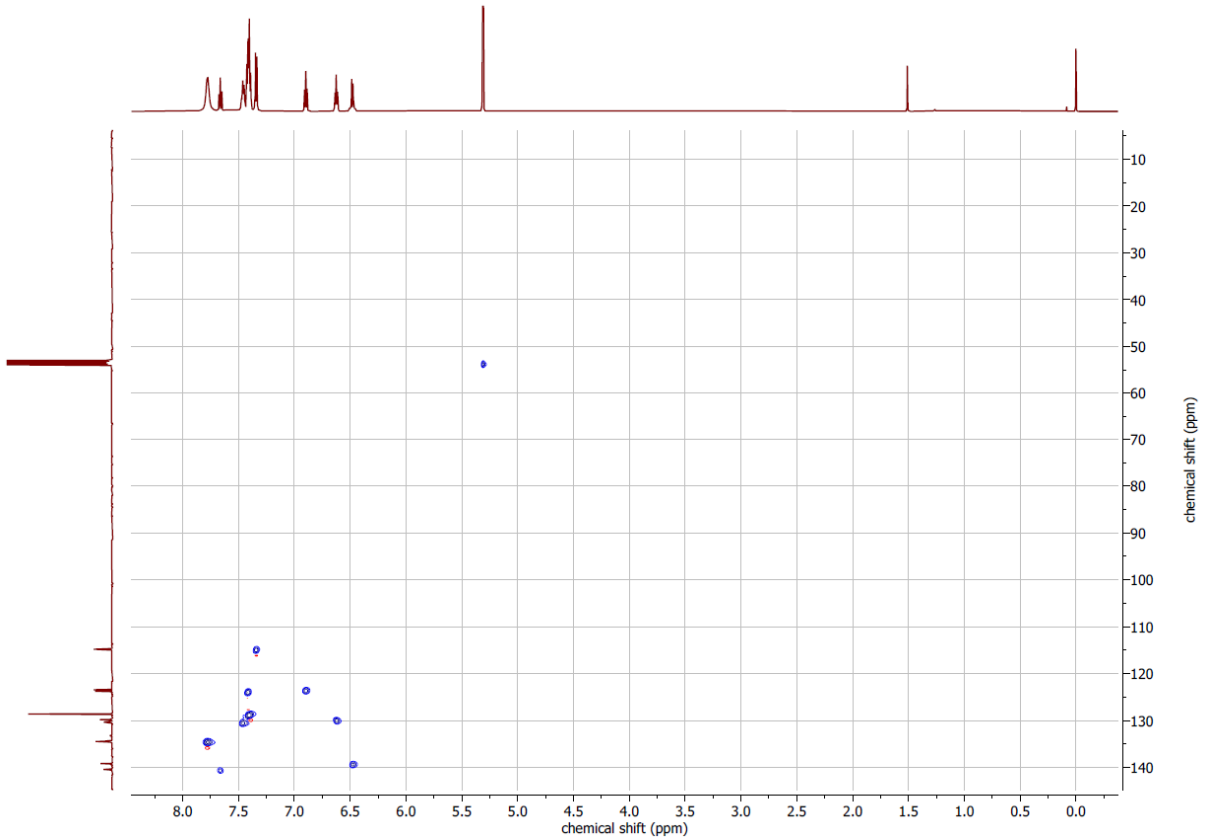

Fig. S4 500 MHz $^{1}H,^{13}C$ HSQC of [Pt(dpp)($AsPh_3$)] in CD_2Cl_2.

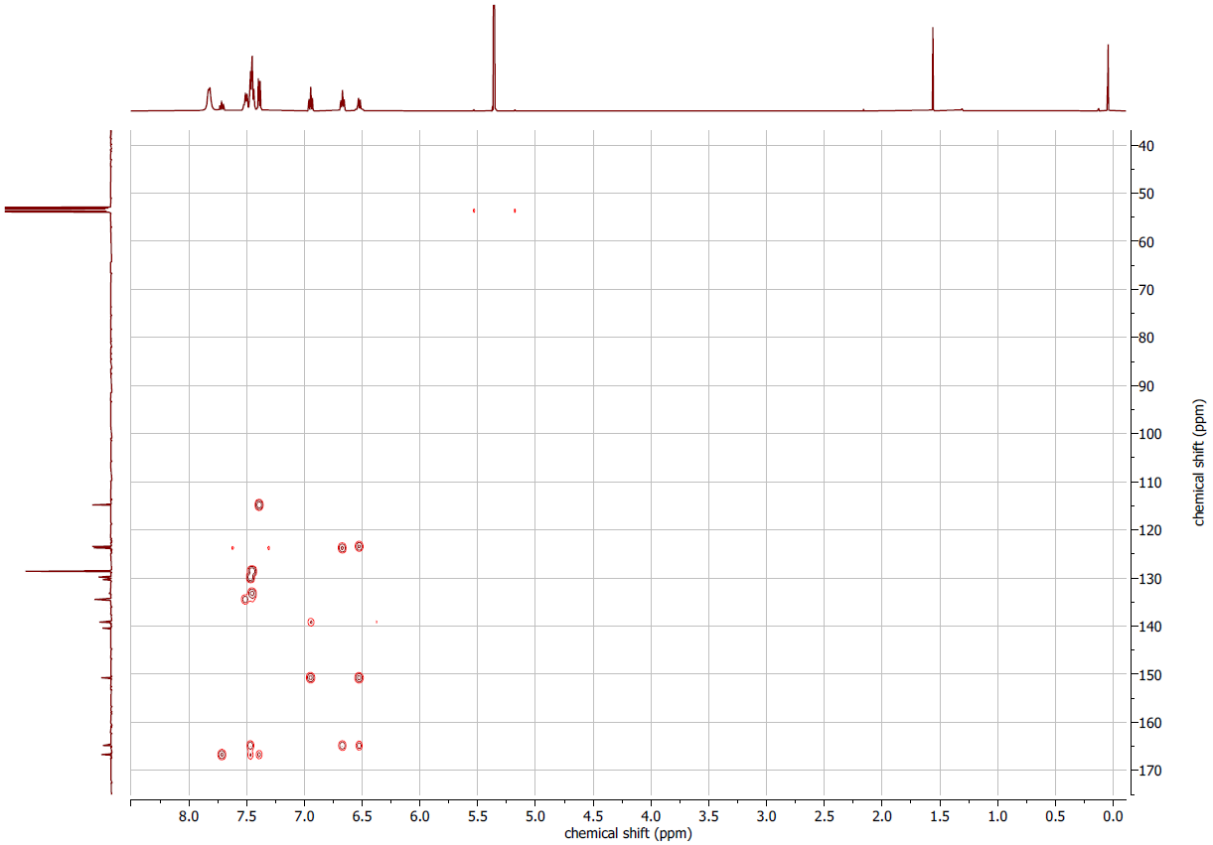

Fig. S5 500 MHz $^{1}H,^{13}C$ HMBC of [Pt(dpp)($AsPh_3$)] in CD_2Cl_2.

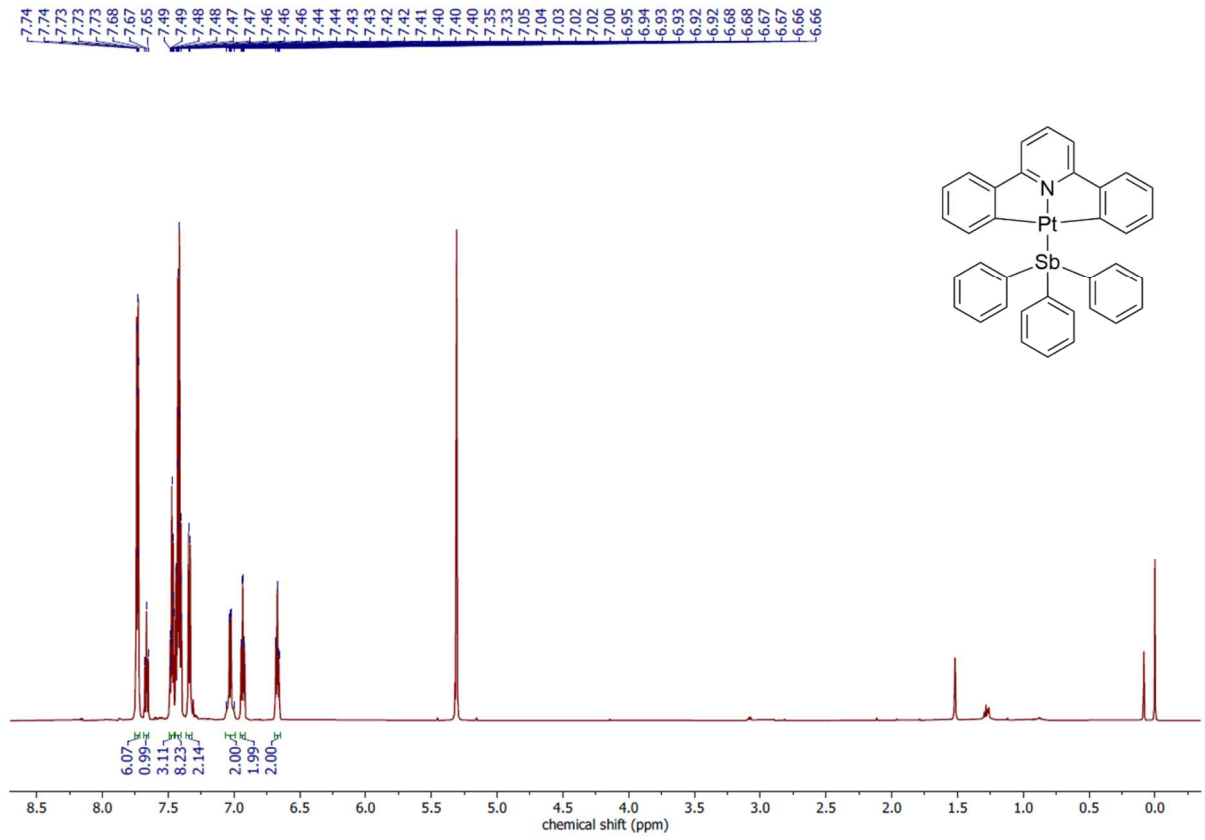

Fig. S6 600 MHz ^{1}H NMR of [Pt(dpp)($SbPh_3$)] in CD_2Cl_2.

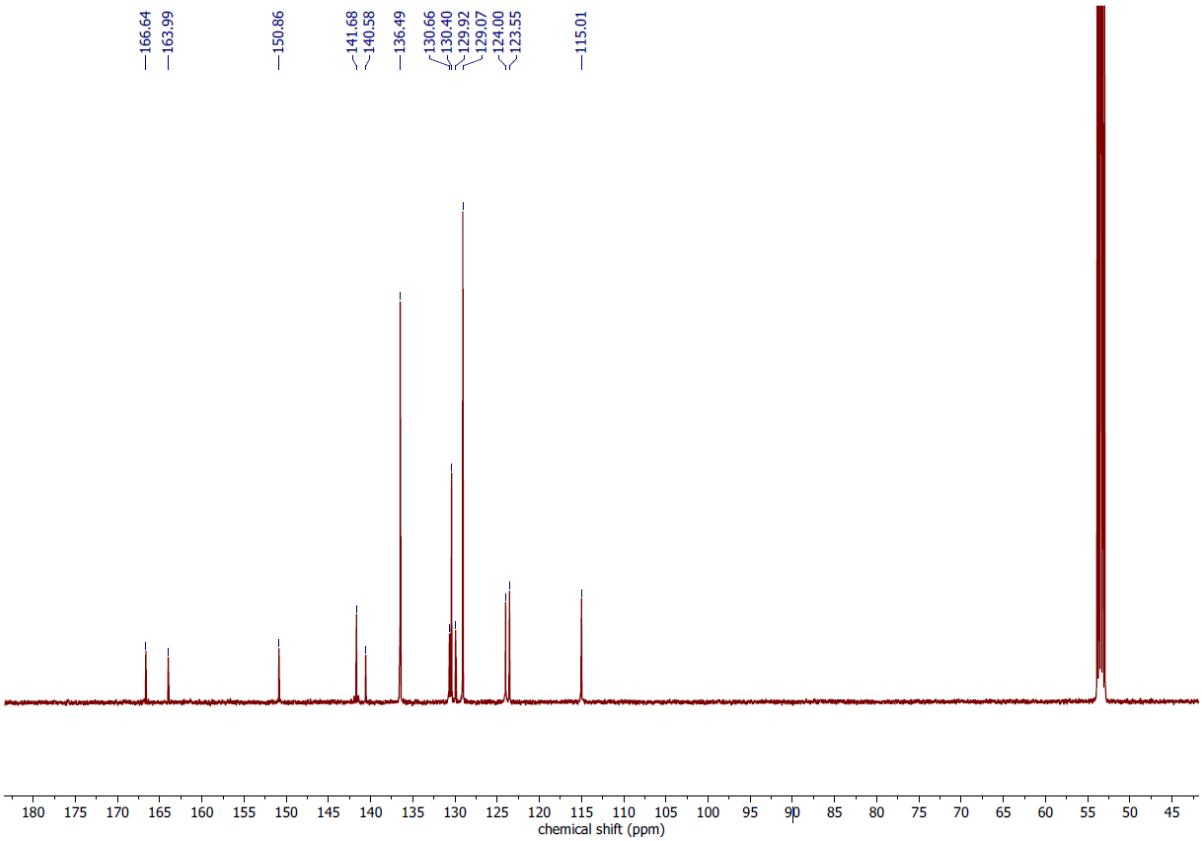

Fig. S7 125 MHz ^{13}C NMR of [Pt(dpp)($SbPh_3$)] in CD_2Cl_2.

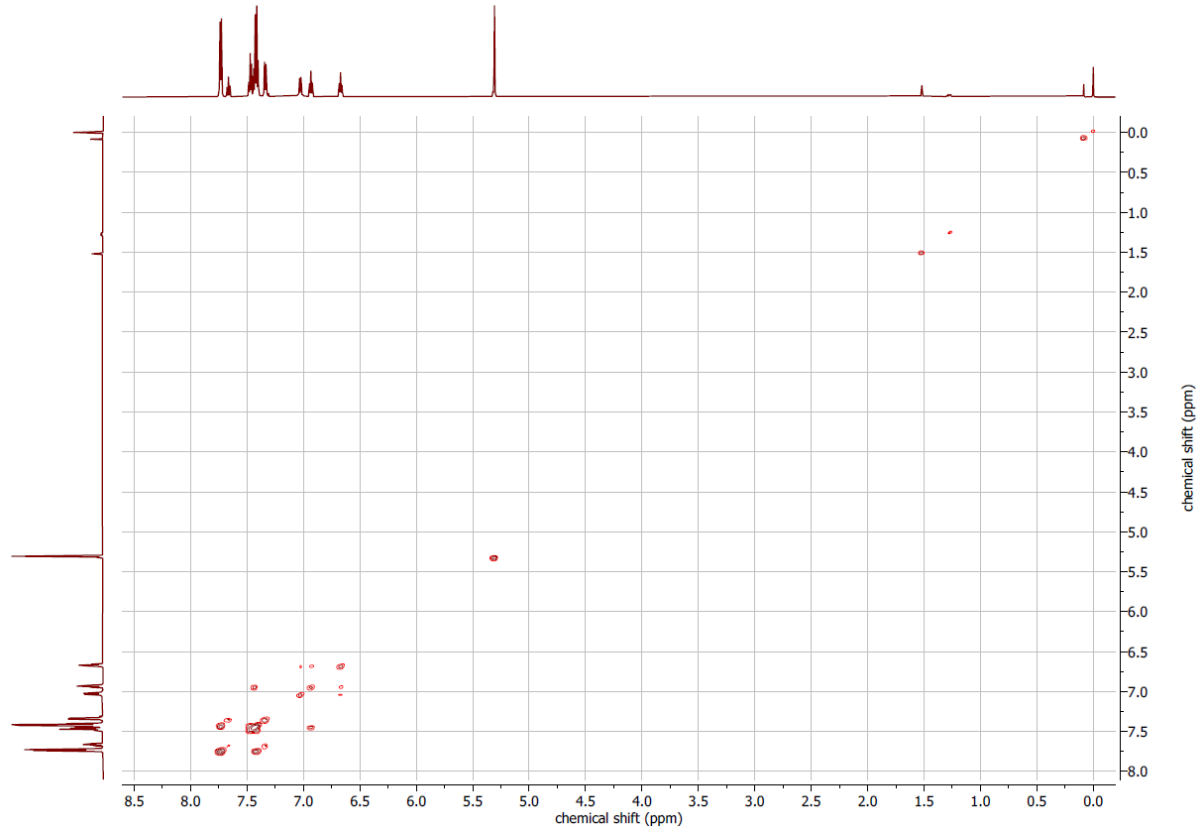

Fig. S8 500 MHz $^{1}H,^{1}H$ COSY of [Pt(dpp)($SbPh_3$)] in CD_2Cl_2.

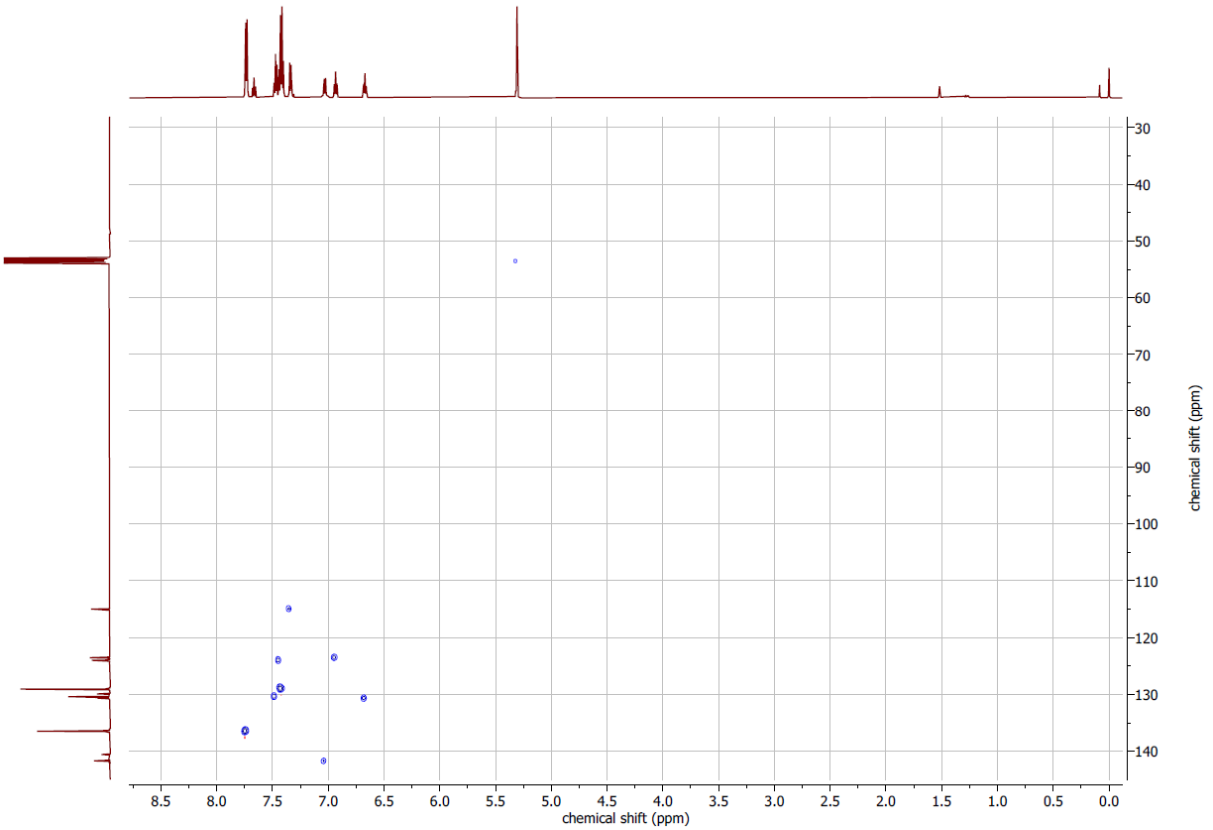

Fig. S9 500 MHz $^{1}H,^{13}C$ HSQC of [Pt(dpp)($SbPh_3$)] in CD_2Cl_2.

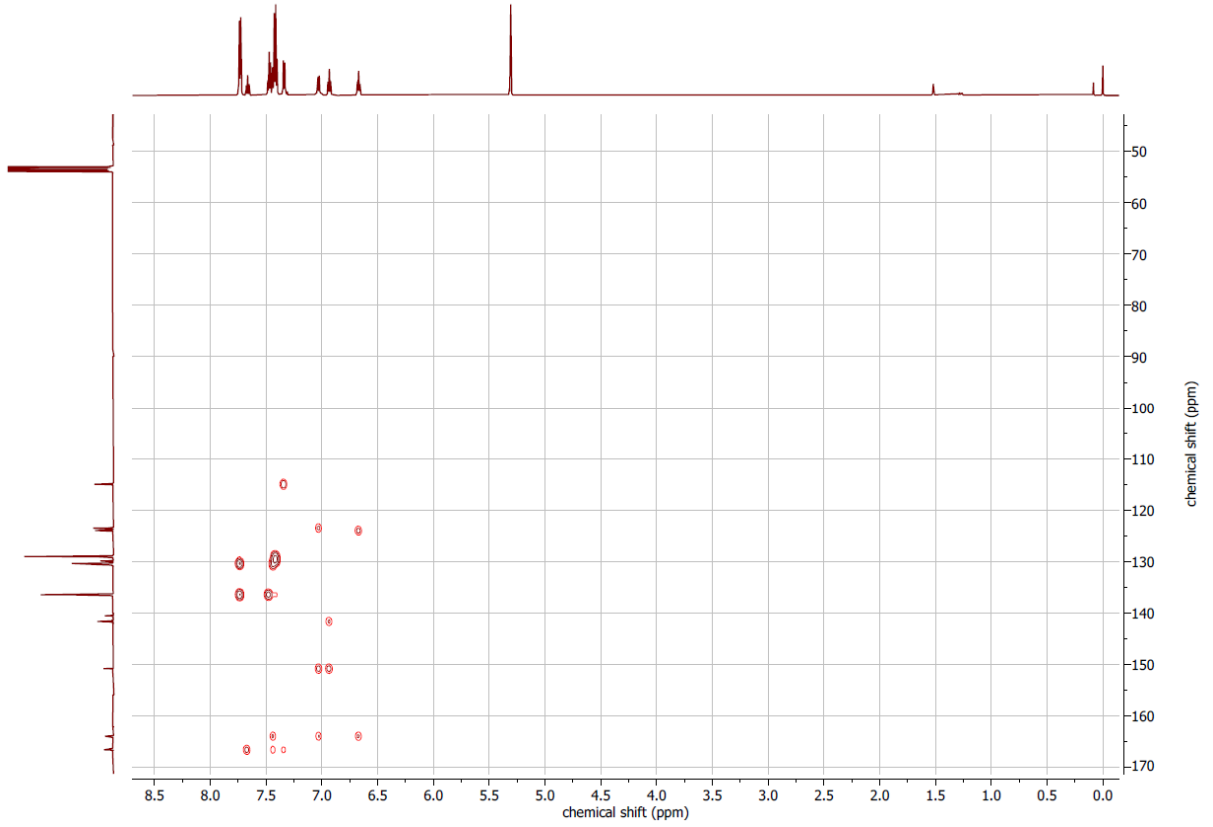

Fig. S10 500 MHz $^{1}H,^{13}C$ HMBC of [Pt(dpp)($SbPh_3$)] in CD_2Cl_2.

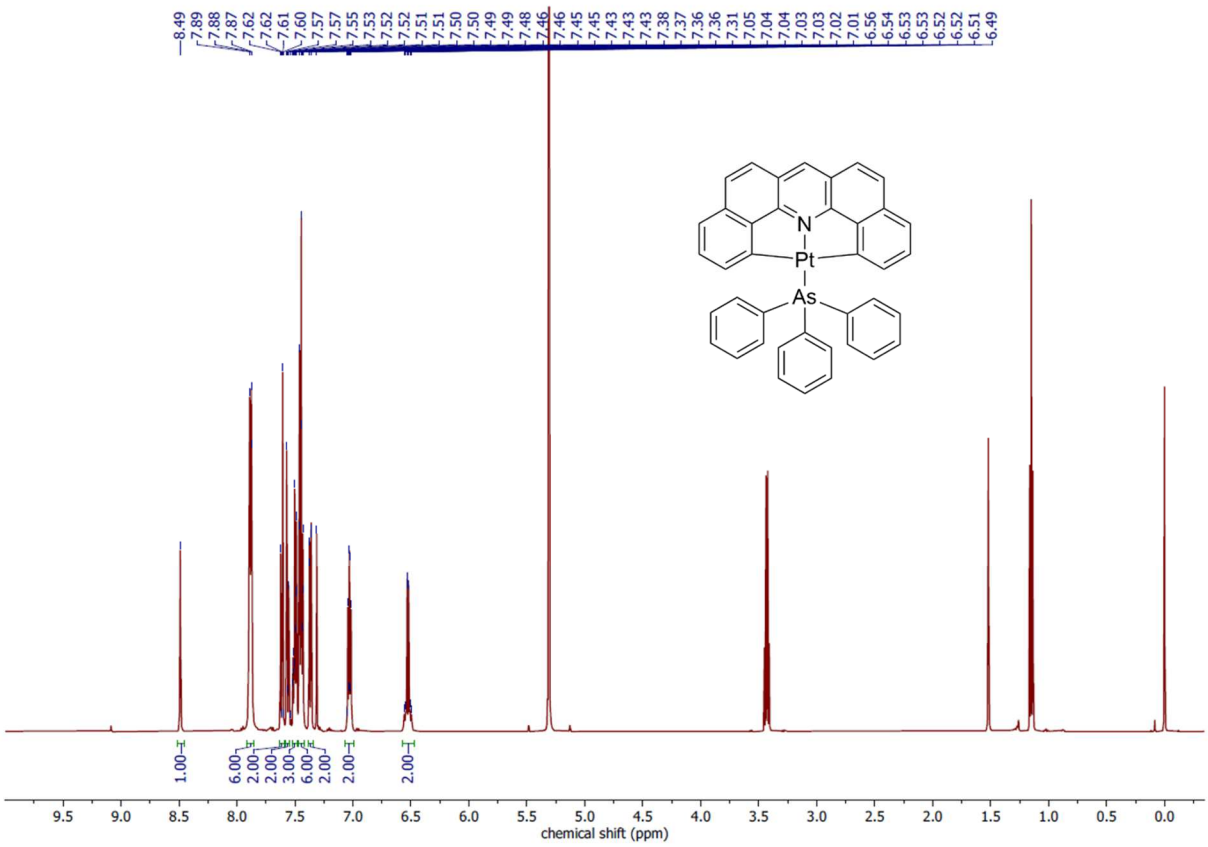

Fig. S11 500 MHz ^{1}H NMR of [Pt(dba)(AsPh$_3$)] in CD_2Cl_2.

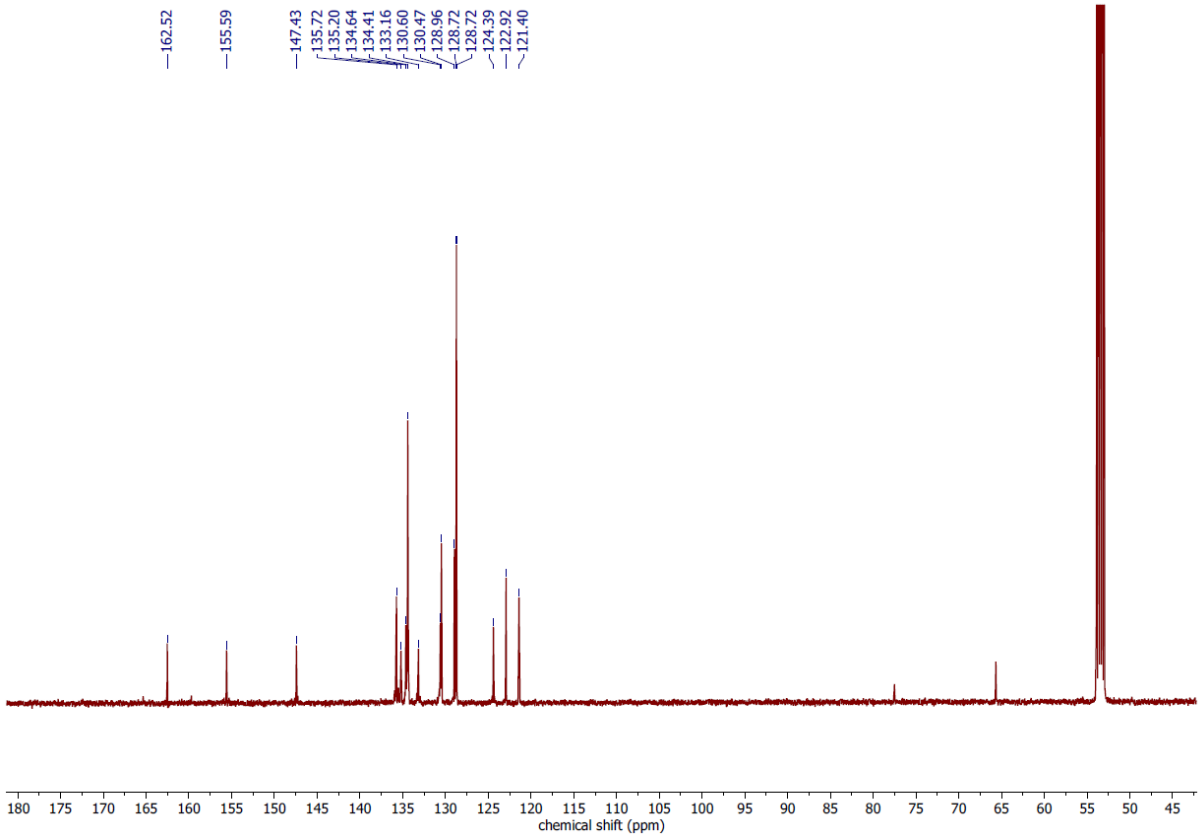

Fig. S12 125 MHz ^{13}C NMR of [Pt(dba)(AsPh$_3$)] in CD_2Cl_2.

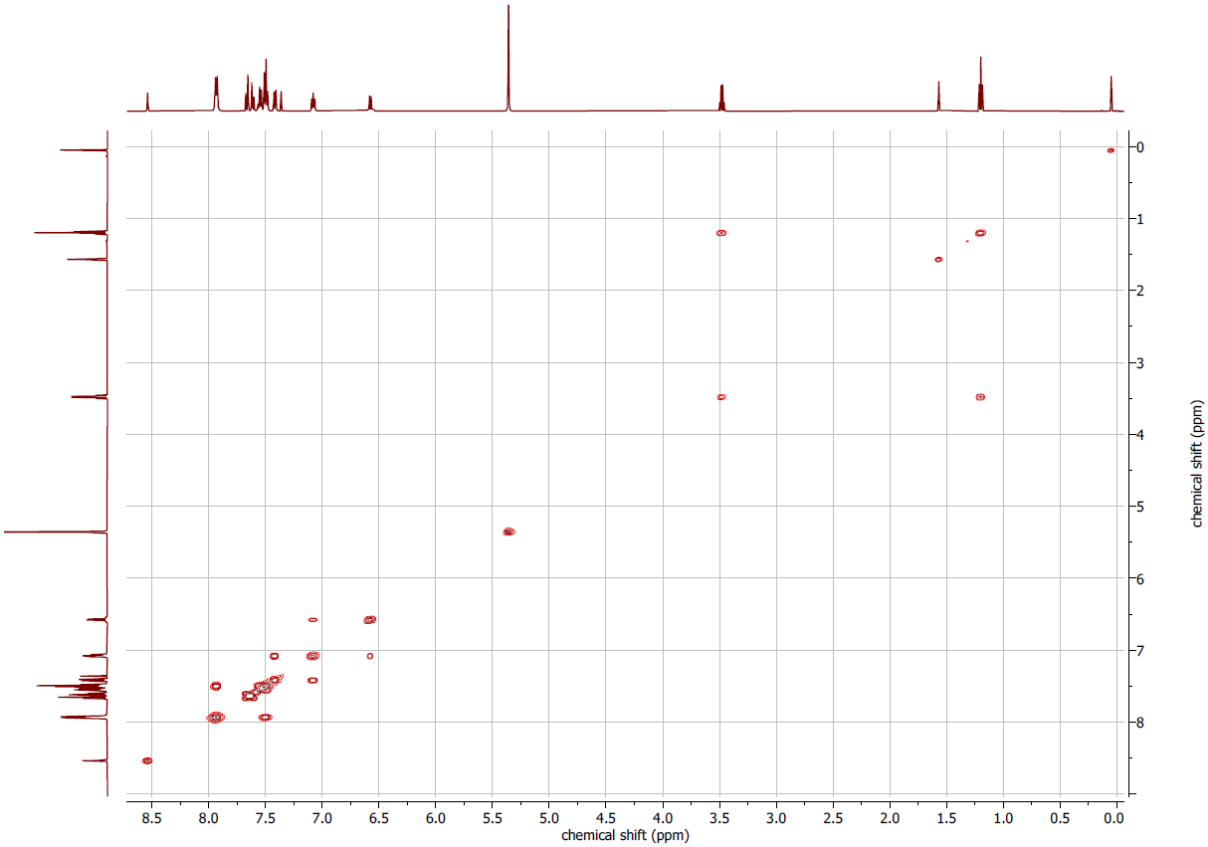

Fig. S13 500 MHz $^{1}H,^{1}H$ COSY of [Pt(dba)($AsPh_3$)] in CD_2Cl_2.

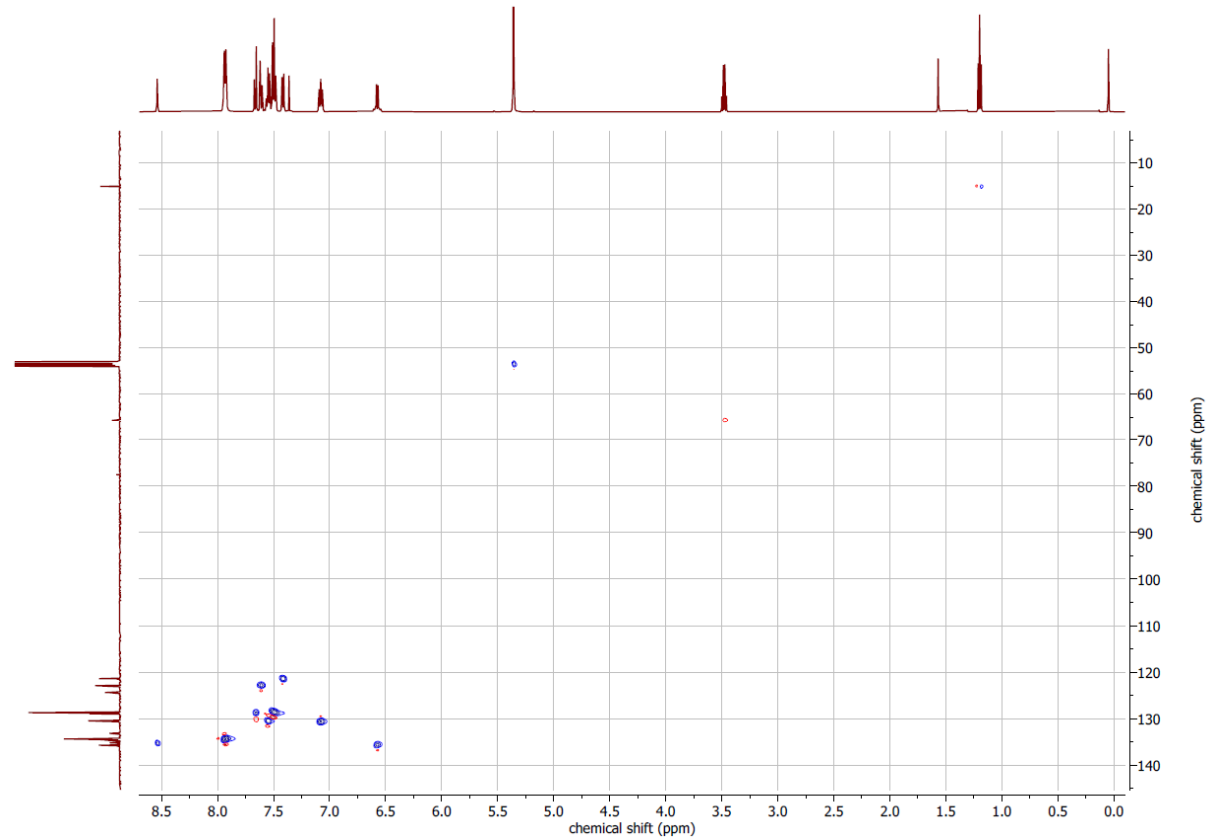

Fig. S14 500 MHz $^{1}H,^{13}C$ HSQC of [Pt(dba)($AsPh_3$)] in CD_2Cl_2.

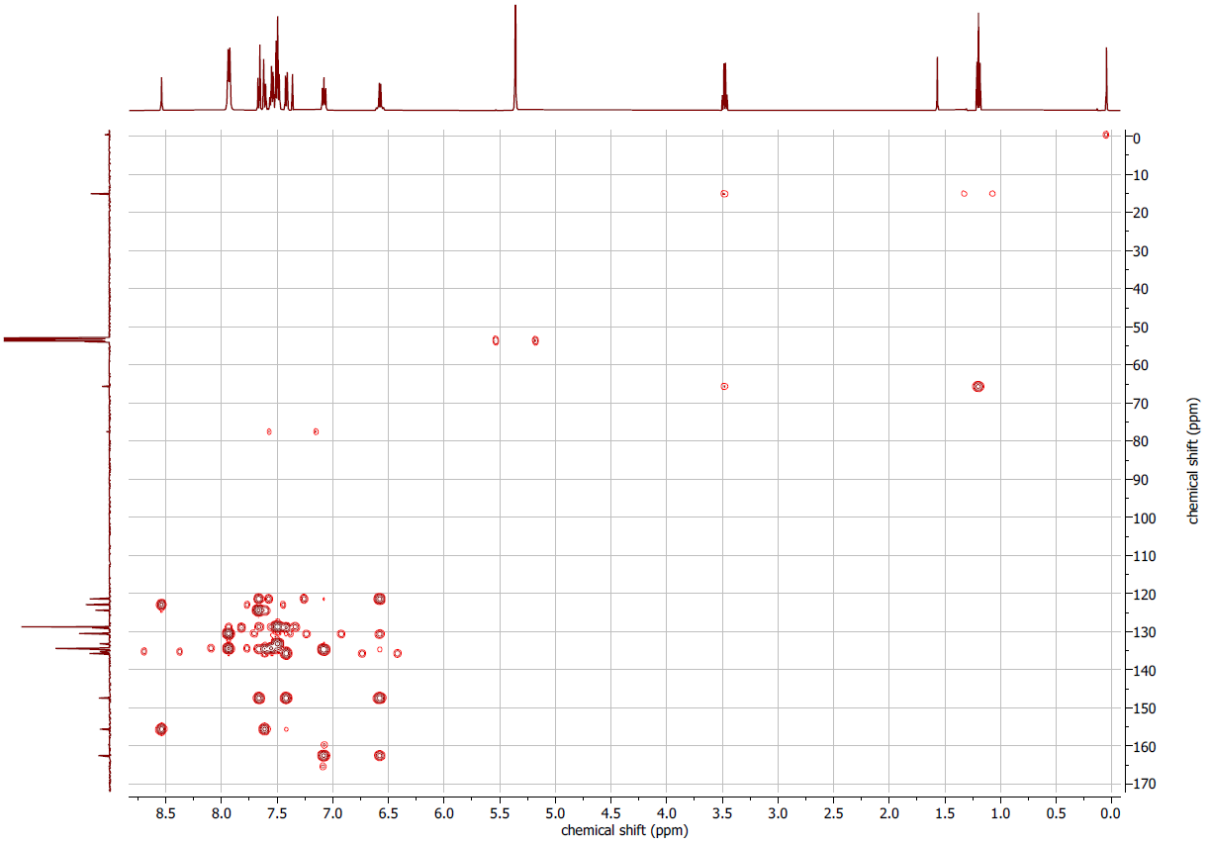

Fig. S15 500 MHz $^{1}H,^{13}C$ HMBC of [Pt(dba)($AsPh_3$)] in CD_2Cl_2.

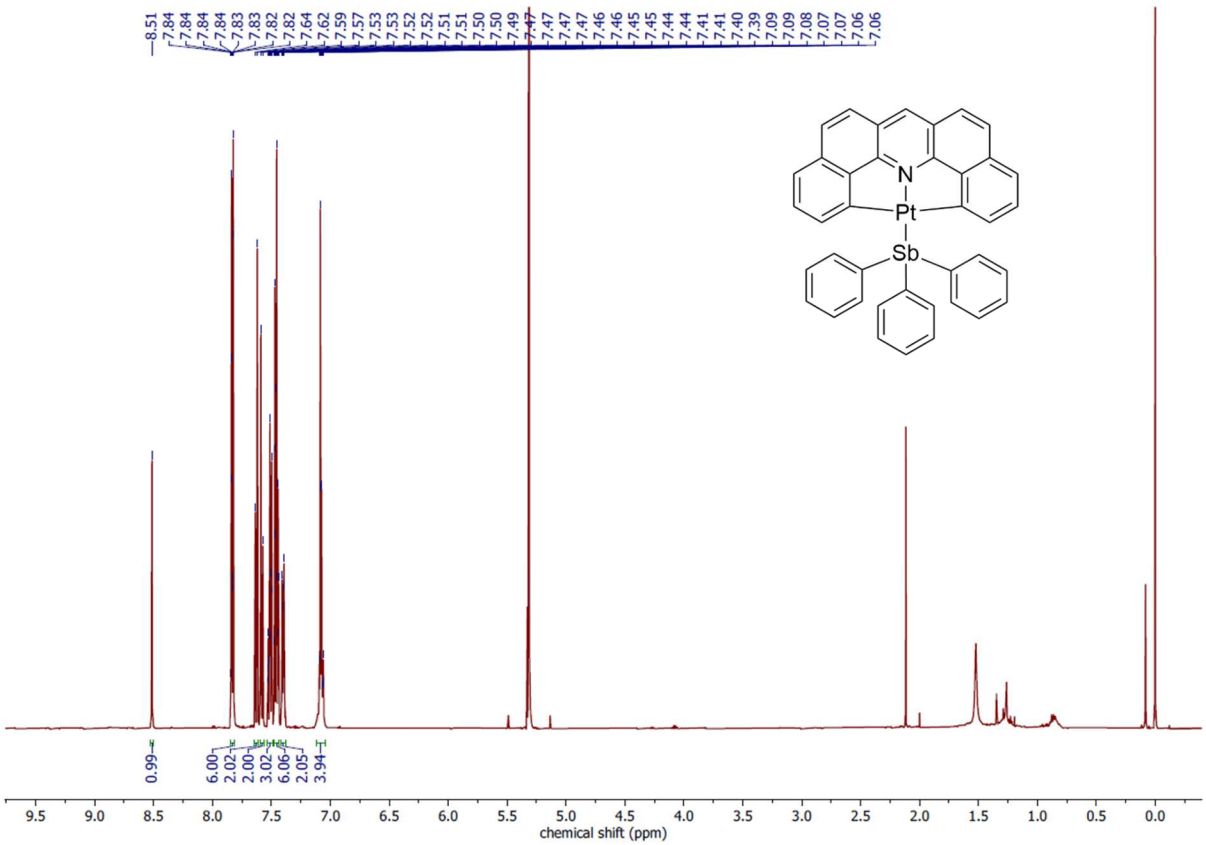

Fig. S16 500 MHz ^{1}H NMR of [Pt(dba)($SbPh_3$)] in CD_2Cl_2.

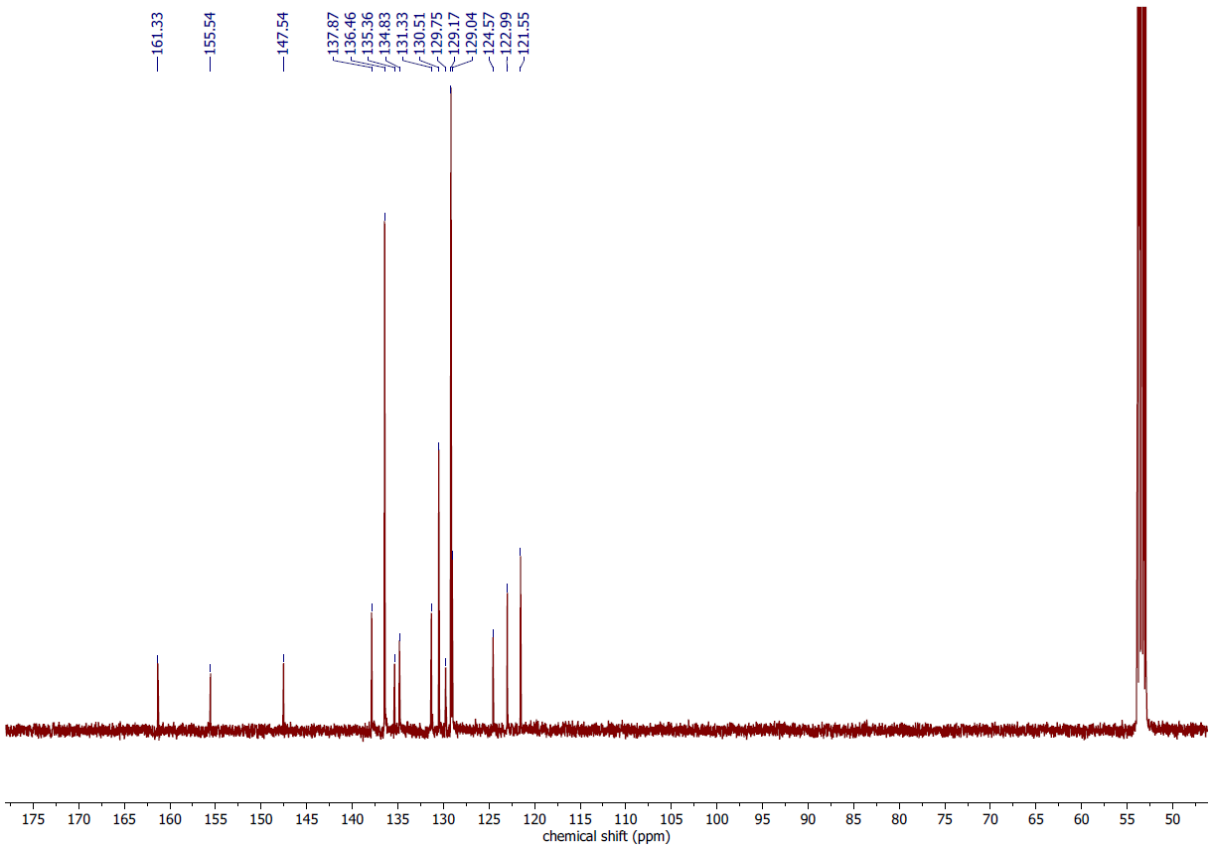

Fig. S17 125 MHz ^{13}C NMR of [Pt(dba)($SbPh_3$)] in CD_2Cl_2.

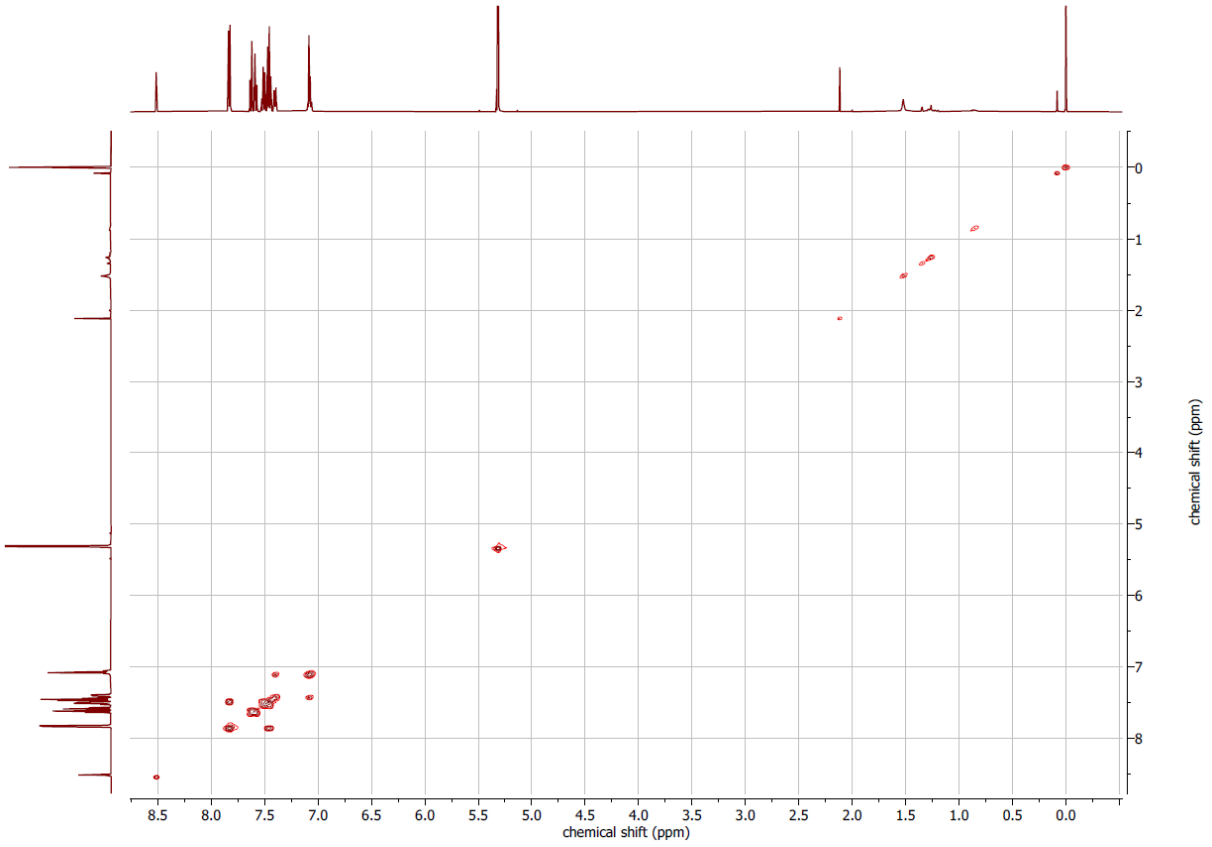

Fig. S18 500 MHz $^{1}H,^{1}H$ COSY of [Pt(dba)($SbPh_3$)] in CD_2Cl_2.

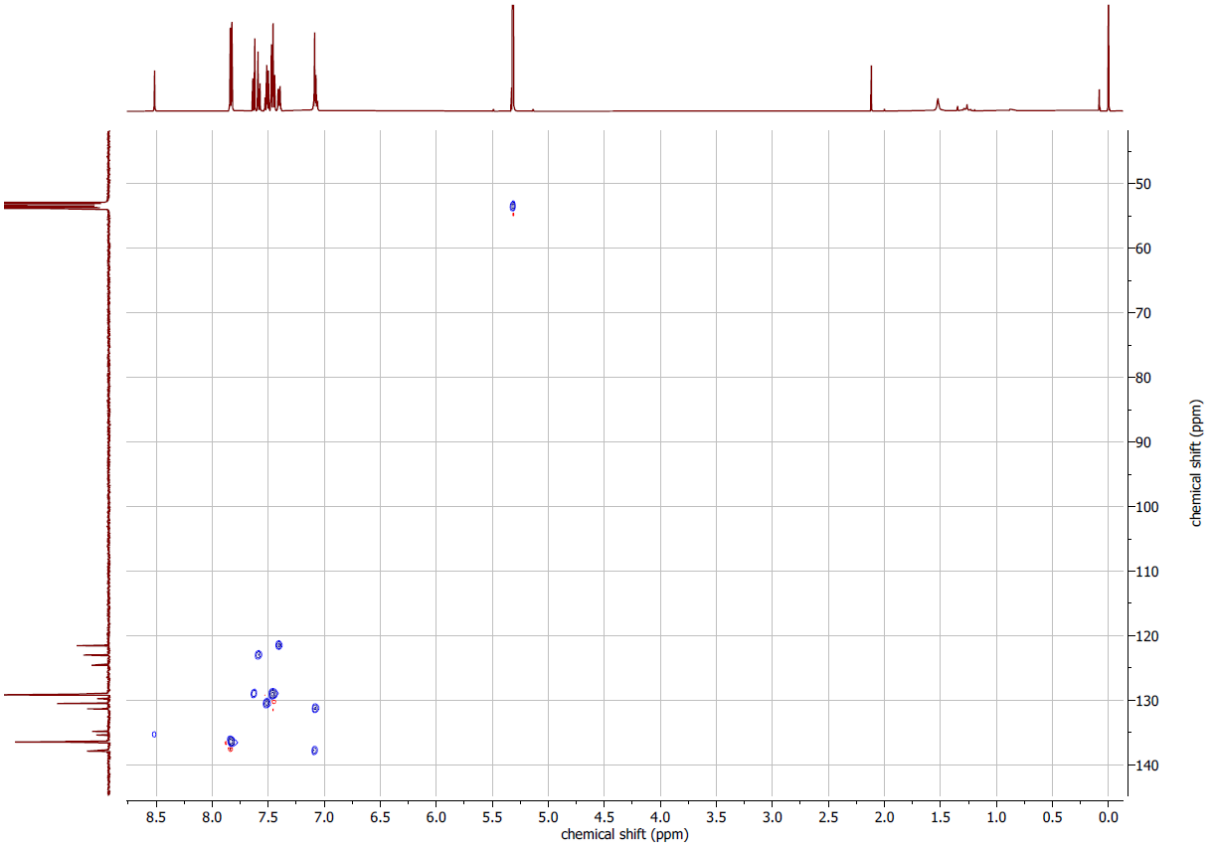

Fig. S19 500 MHz $^{1}H,^{13}C$ HSQC of [Pt(dba)($SbPh_3$)] in CD_2Cl_2.

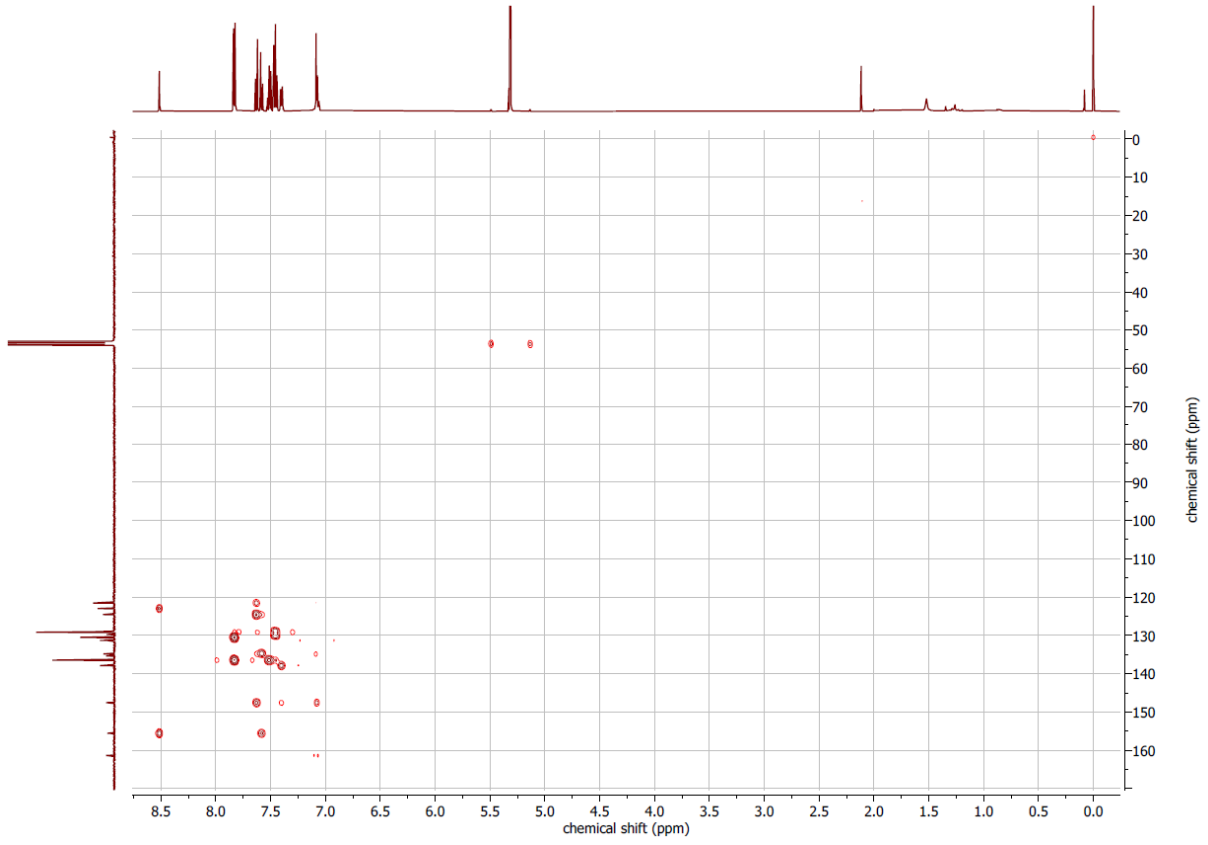

Fig. S20 500 MHz $^{1}H,^{13}C$ HMBC of [Pt(dba)($SbPh_3$)] in CD_2Cl_2.

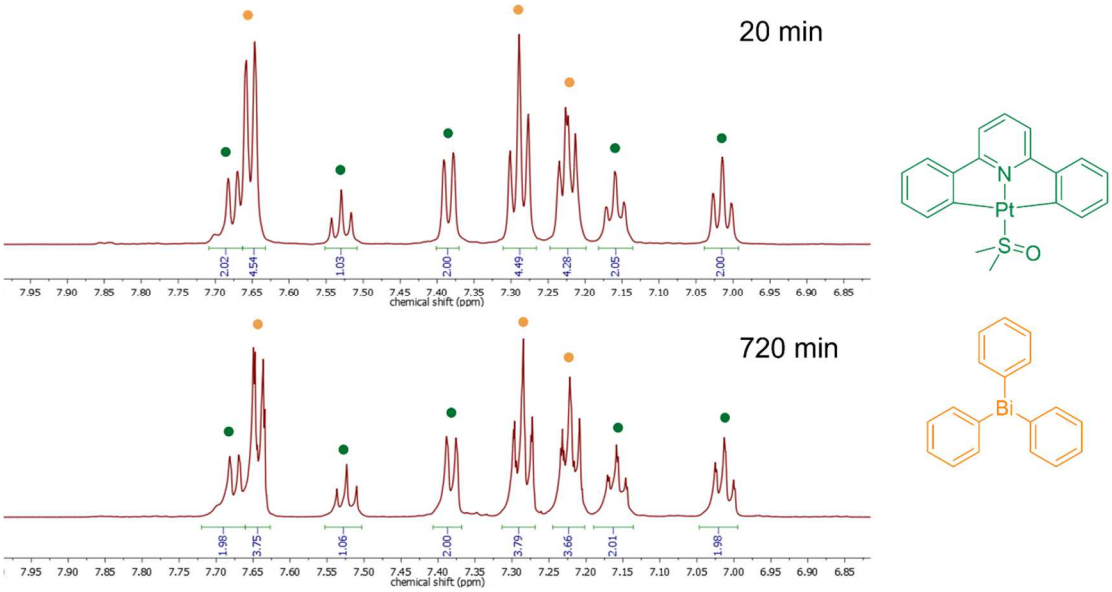

Fig. S21 600 MHz ^{1}H NMR spectra from *in situ* NMR observation of a mixture of [Pt(dpp)(dmso)] and $BiPh_3$ in CD_2Cl_2.

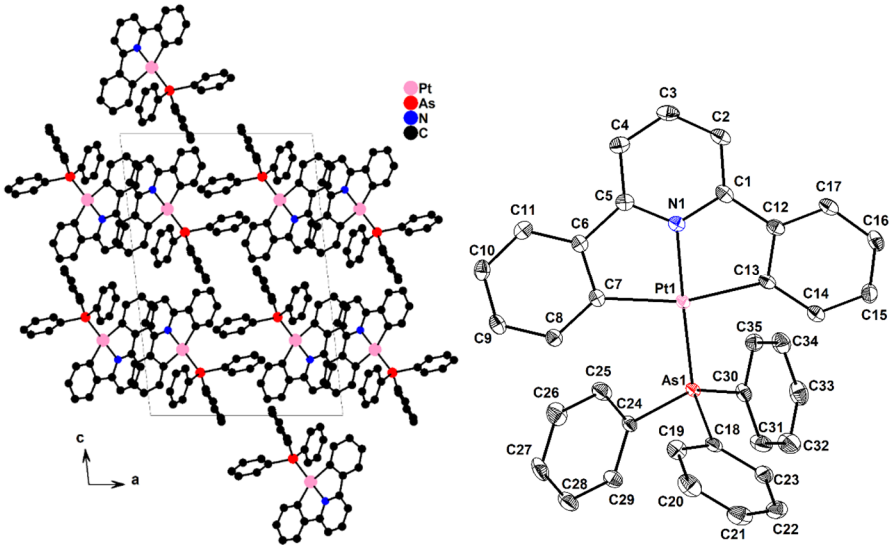

Fig. S22 Crystal structure (left) of [Pt(dpp)($AsPh_3$)] viewed along the *b* axis and molecular structure (right) with 50% ellipsoids, H atoms omitted for clarity.

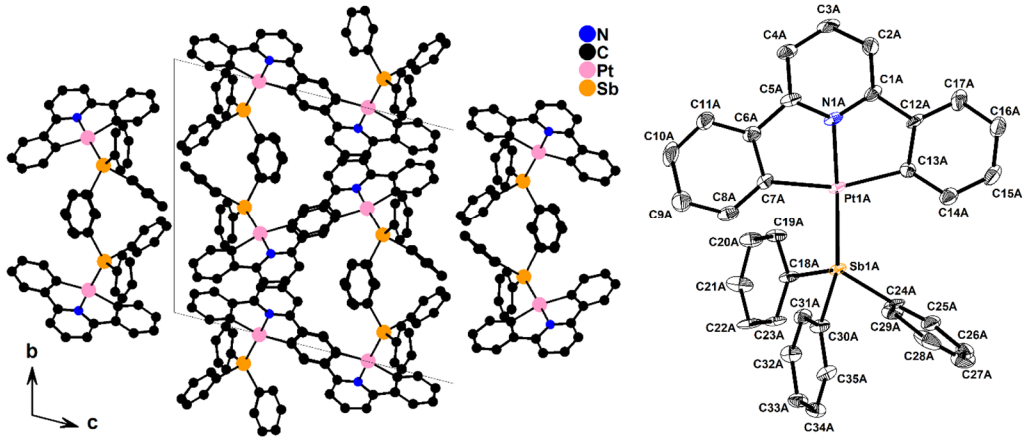

Fig. S23 Crystal structure (left) of [Pt(dpp)($SbPh_3$)] viewed along the *a* axis and molecular structure (right) with 50% ellipsoids, H atoms omitted for clarity.

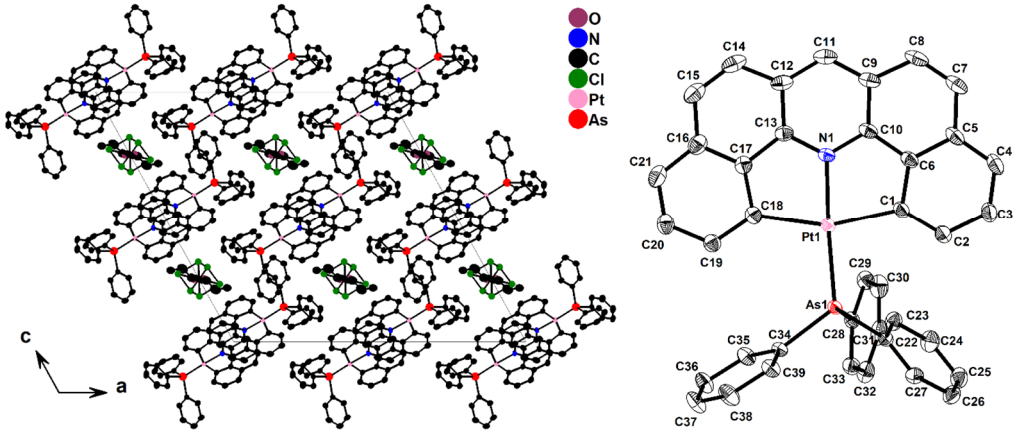

Fig. S24 Crystal structure (left) of [Pt(dba)(AsPh$_3$)]·Et$_2$O·CHCl$_3$ viewed along the *b* axis and molecular structure of [Pt(dbaAsPh$_3$] (right) with 50% ellipsoids, H atoms and co-crystallised solvent molecules omitted for clarity.

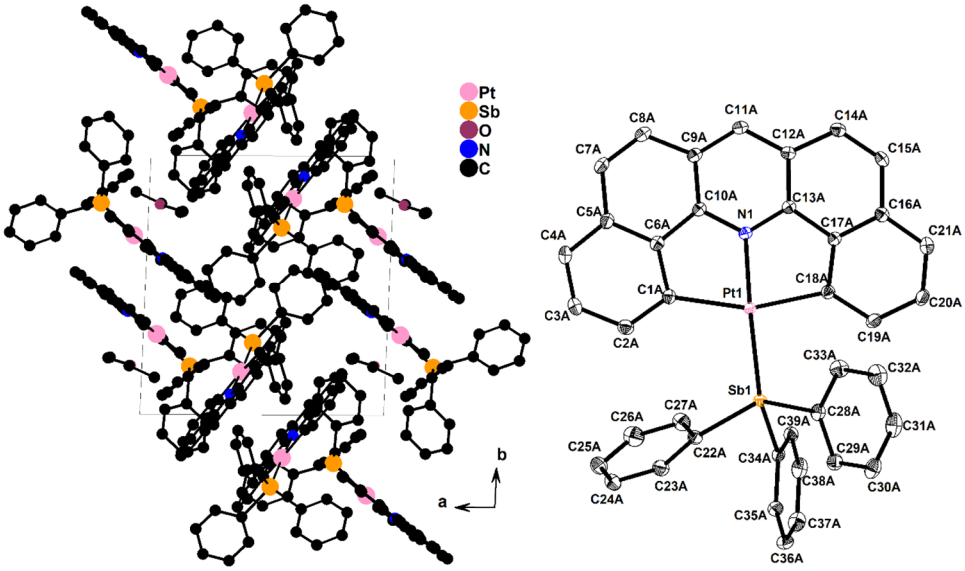

Fig. S25 Crystal structure (left) of [Pt(dba)(SbPh$_3$)]·0.5Et$_2$O viewed along the *c* axis and molecular structure of [Pt(dba)(SbPh$_3$)] (right) with 50% ellipsoids, H atoms and co-crystallised solvent molecules omitted for clarity.

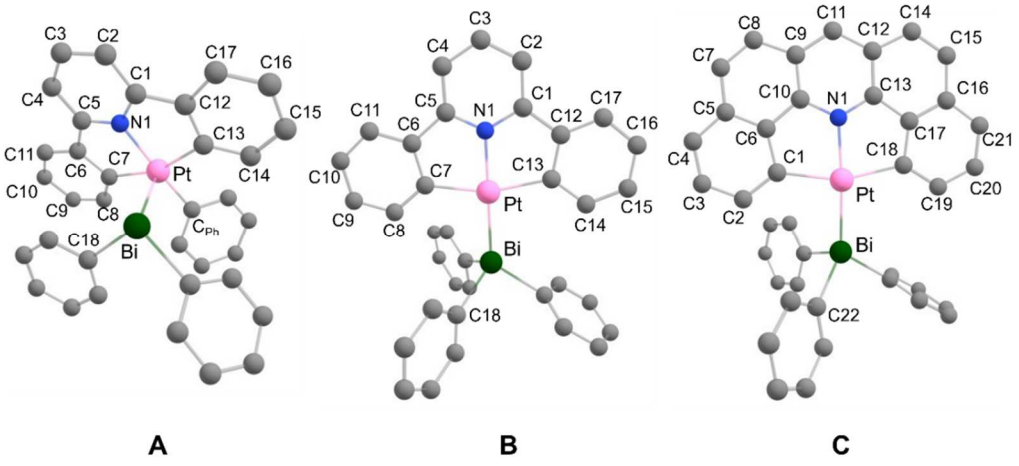

Fig. S26 Structures of [Pt(dpp)(BiPh$_3$)] and [Pt(dba)(BiPh$_3$)] from free (left) and constrained (middle and right) DFT geometry optimisations.

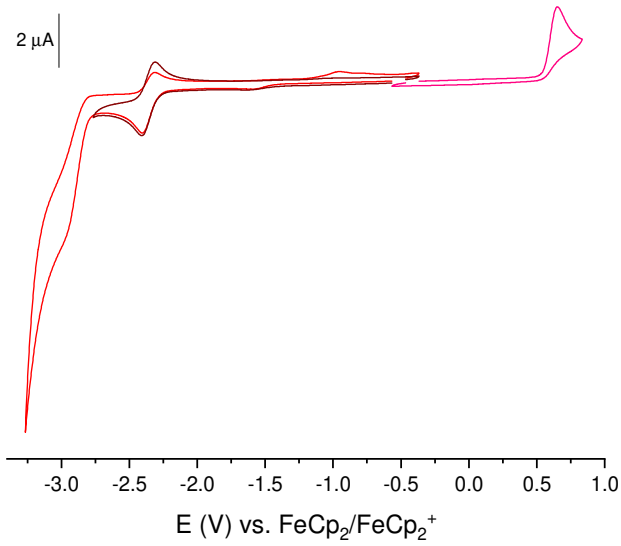

Fig. S27 Cyclic voltammograms of [Pt(dpp)(PPh_3)] in 0.1 M *n*-Bu_4NPF_6/THF.

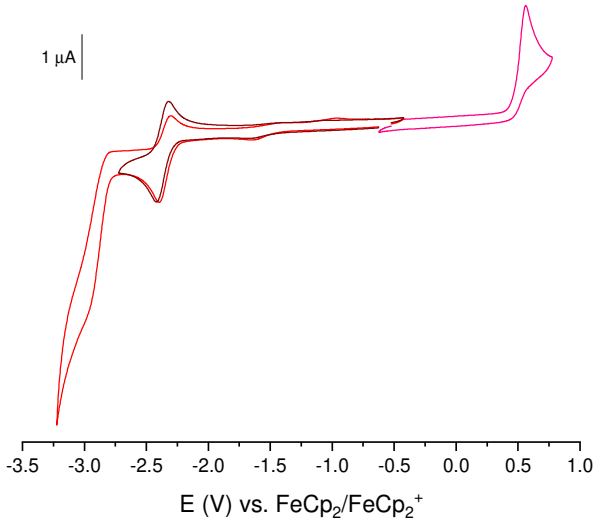

Fig. S28 Cyclic voltammograms of [Pt(dpp)($AsPh_3$)] in 0.1 M *n*-Bu_4NPF_6/THF.

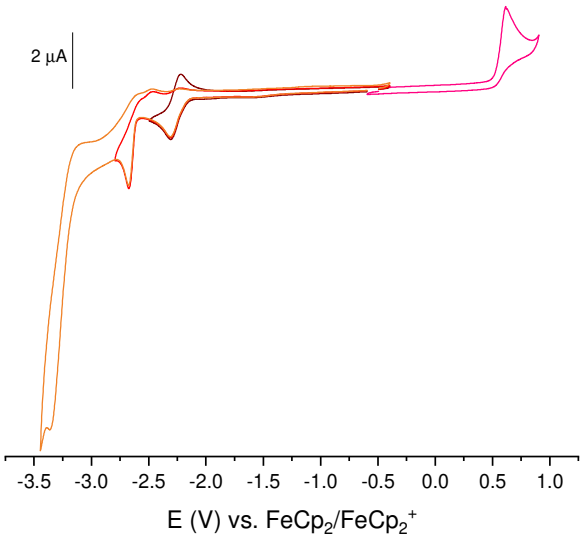

Fig. S29 Cyclic voltammograms of [Pt(dpp)($SbPh_3$)] in 0.1 M *n*-Bu_4NPF_6/THF.

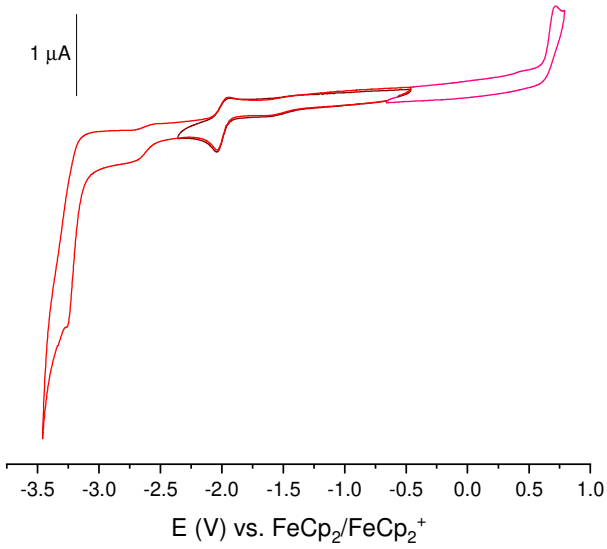

Fig. S30 Cyclic voltammograms of [Pt(dba)(PPh_3)] in 0.1 M *n*-Bu_4NPF_6/THF.

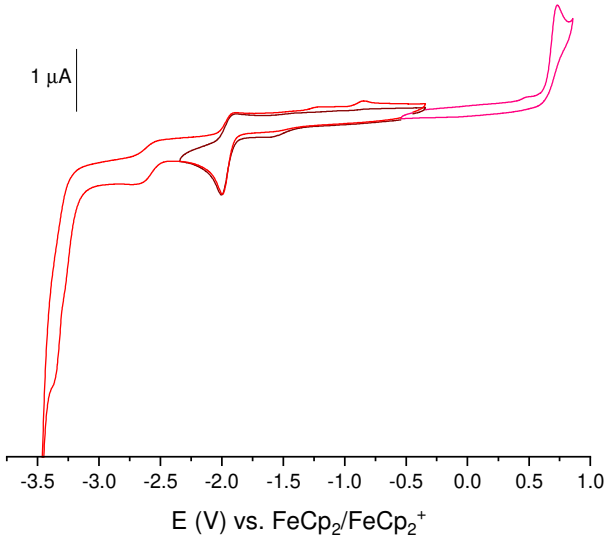

Fig. S31 Cyclic voltammograms of [Pt(dba)($AsPh_3$)] in 0.1 M *n*-Bu_4NPF_6/THF.

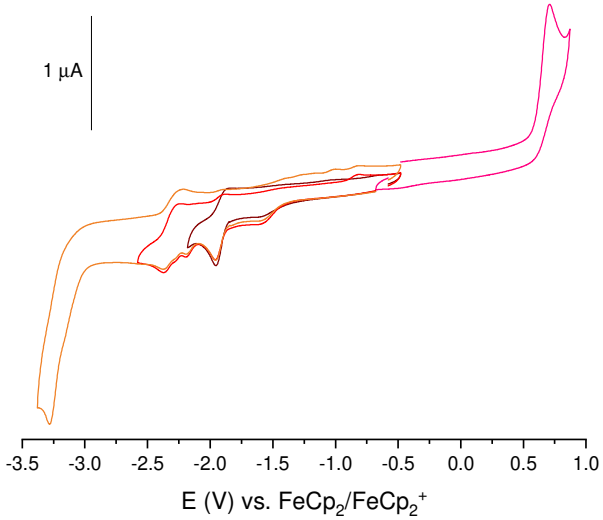

Fig. S32 Cyclic voltammograms of [Pt(dba)($SbPh_3$)] in 0.1 M *n*-Bu_4NPF_6/THF.

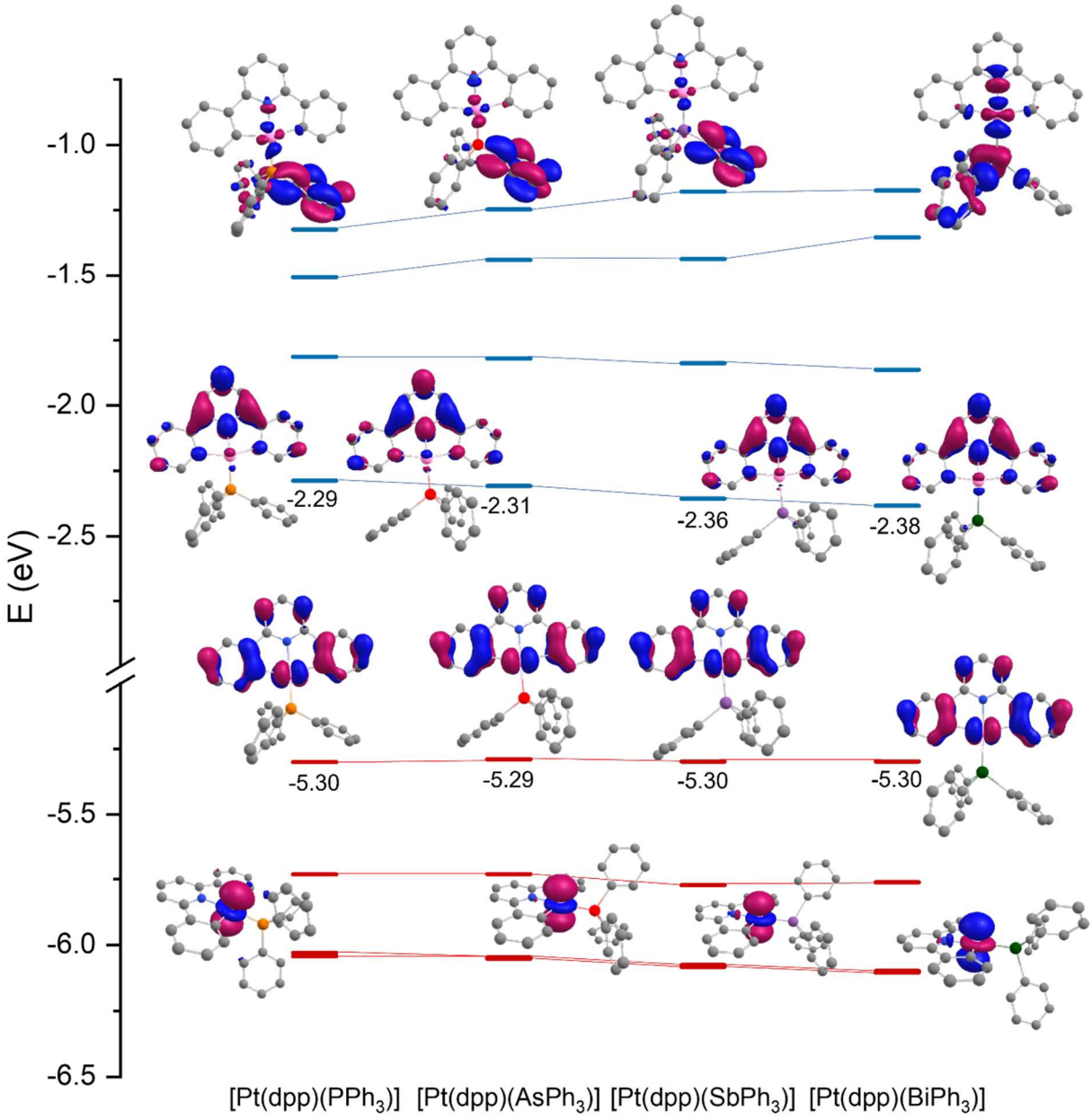

Fig. S33 Selected DFT-calculated frontier orbitals and energies for [Pt(dpp)(PnPh3)] (Pn = P, As, Sb, Bi).

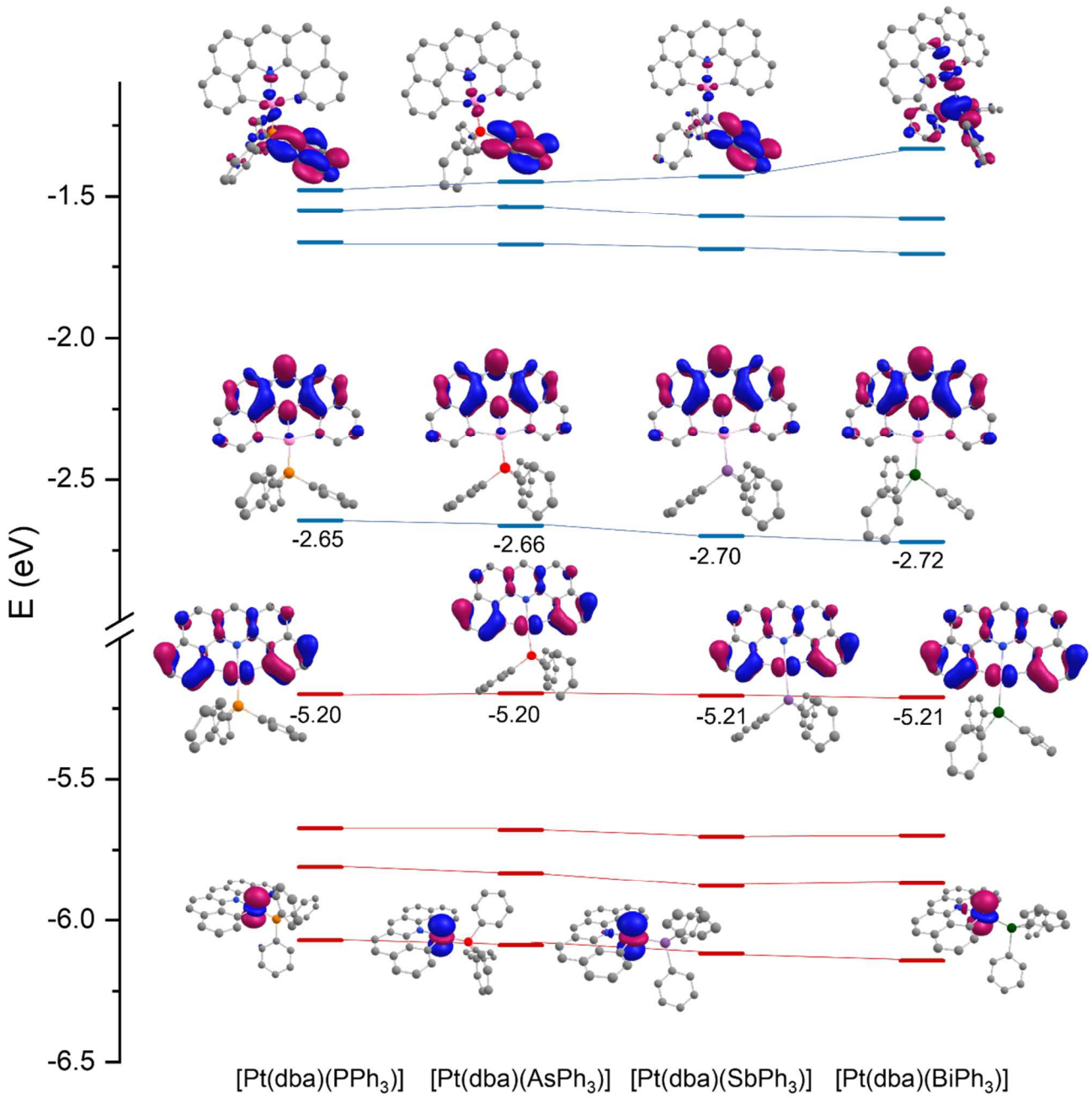

Fig. S34 Selected DFT-calculated frontier orbitals and energies for [Pt(dba)(PnPh3)] (Pn = P, As, Sb, Bi).

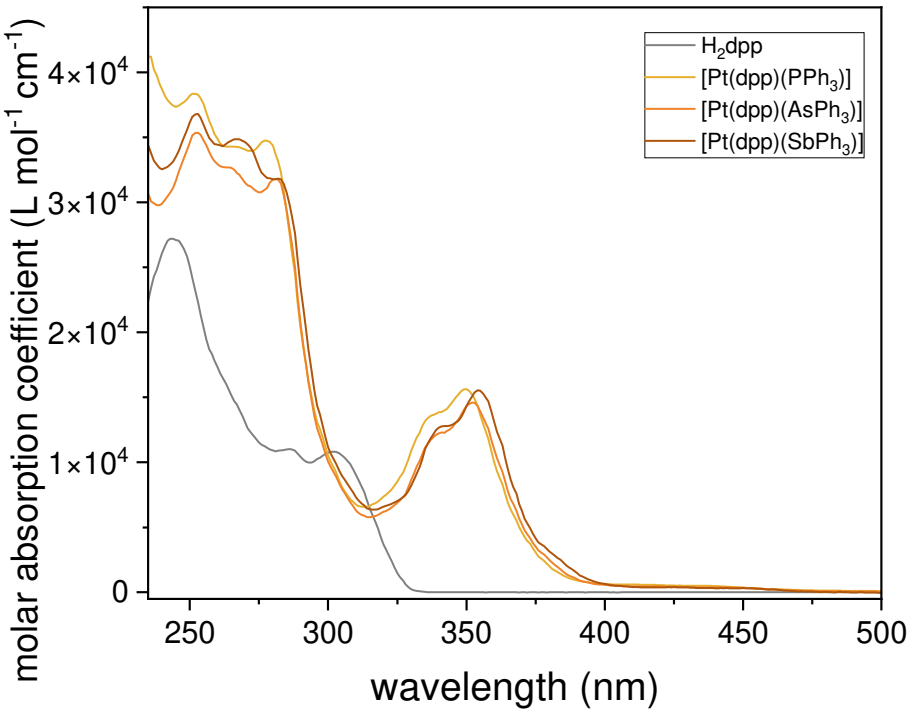

Fig. S35 Experimental UV-vis absorption spectra of H_2dpp, and the complexes [Pt(dpp)(PnPh$_3$)] (Pn = P, As, and Sb) in CH_2Cl_2 solution at 298 K.

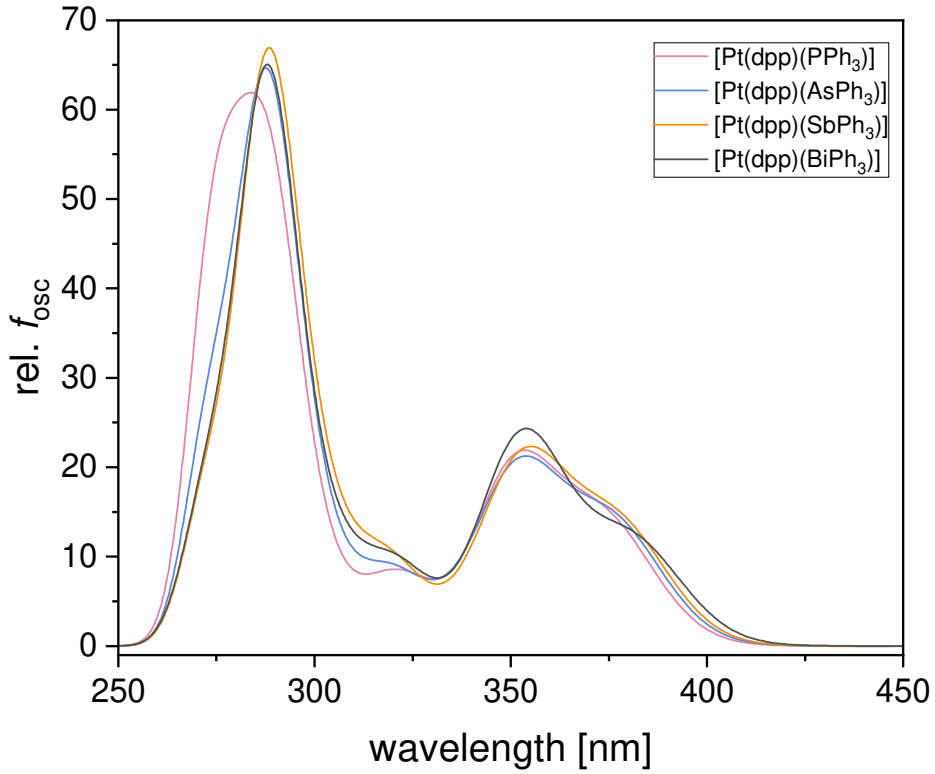

Fig. S36 TD-DFT calculated (TPSSh/def2-TZVP/CPCM(CH_2Cl_2)) UV-vis absorption spectra of the complexes [Pt(dpp)(PnPh$_3$)] (Pn = P, As, Sb, Bi).

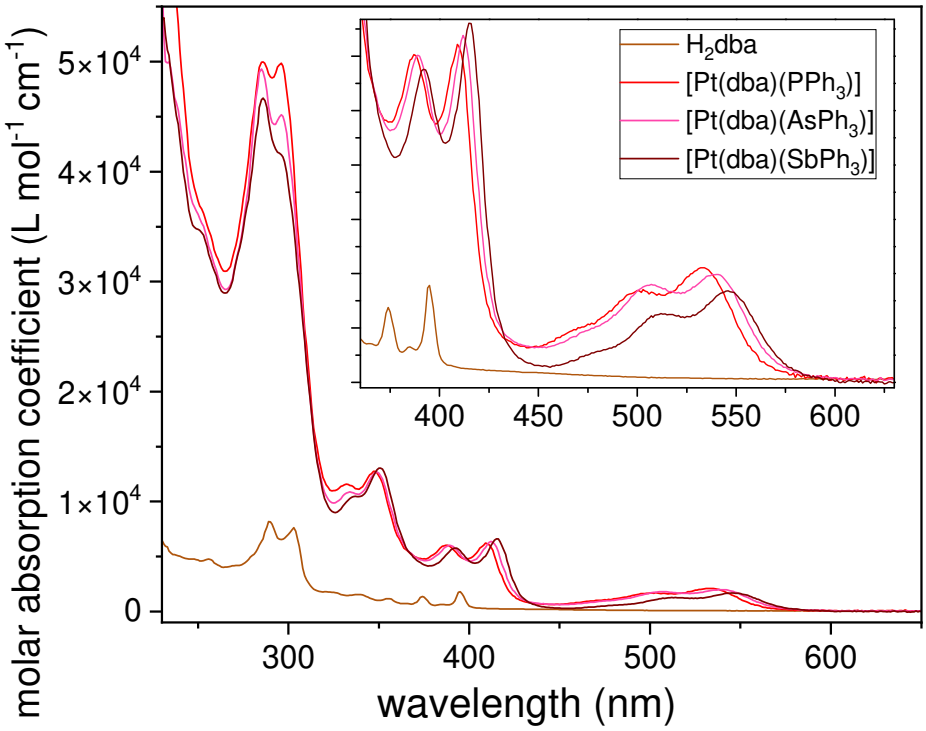

Fig. S37 Experimental UV-vis absorption spectra of H_2dba, and the complexes [Pt(dba)($PnPh_3$)] (Pn = P, As, and Sb) in CH_2Cl_2 solution at 298 K.

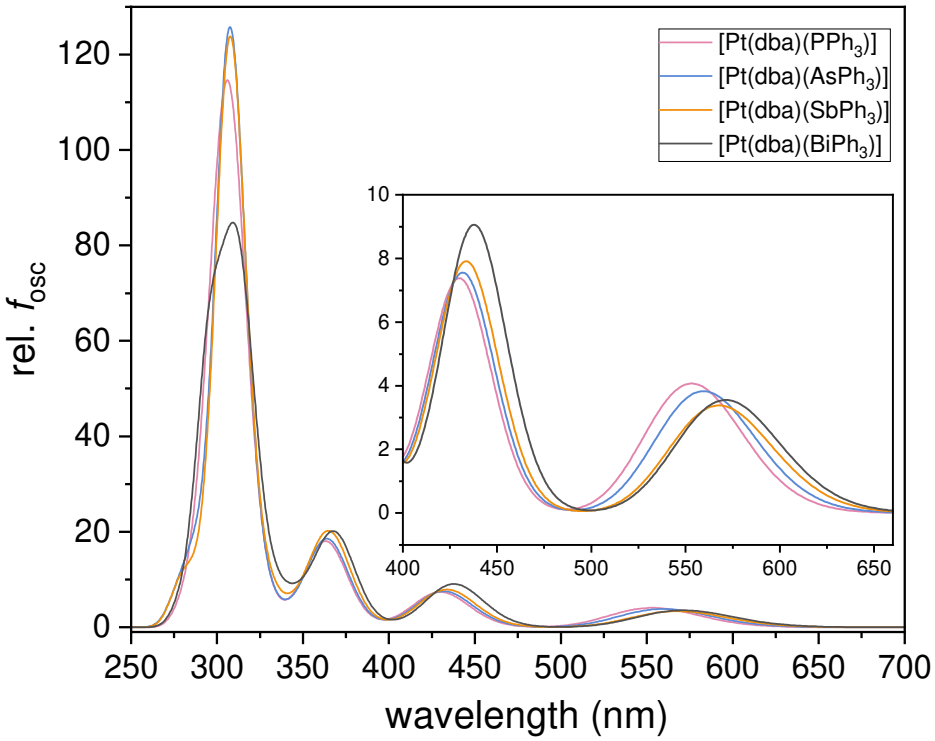

Fig. S38 TD-DFT-calculated (TPSSh/def2-TZVP/CPCM(CH_2Cl_2)) UV-vis absorption spectra of [Pt(dba)($PnPh_3$)] (Pn = P, As, Sb, Bi).

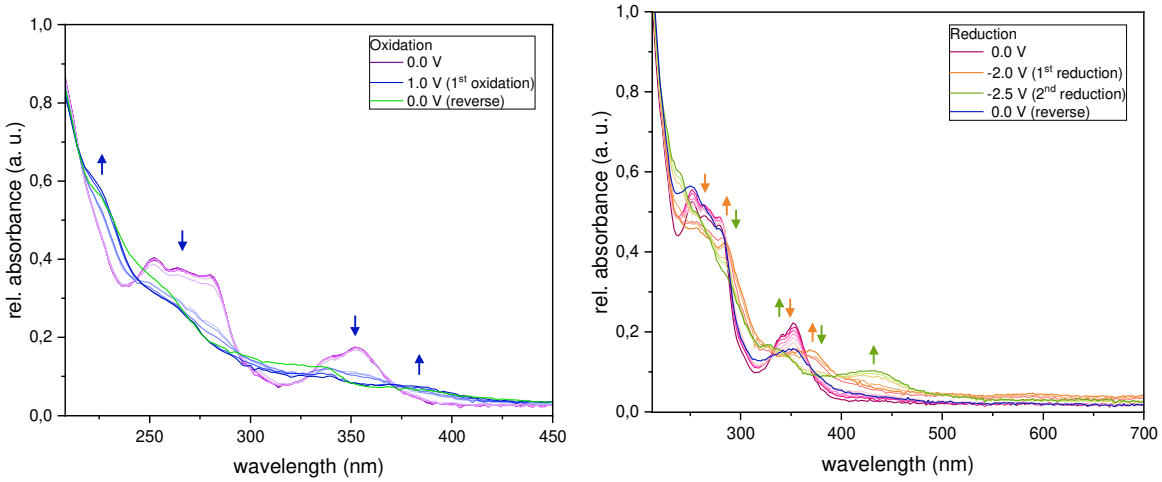

Fig. S39 UV-vis absorption spectra of [Pt(dpp)($AsPh_3$)] during anodic (left) and cathodic (right) electrolysis (spectroelectrochemistry) in 0.1 M *n*-Bu_4NPF_6 THF solution.

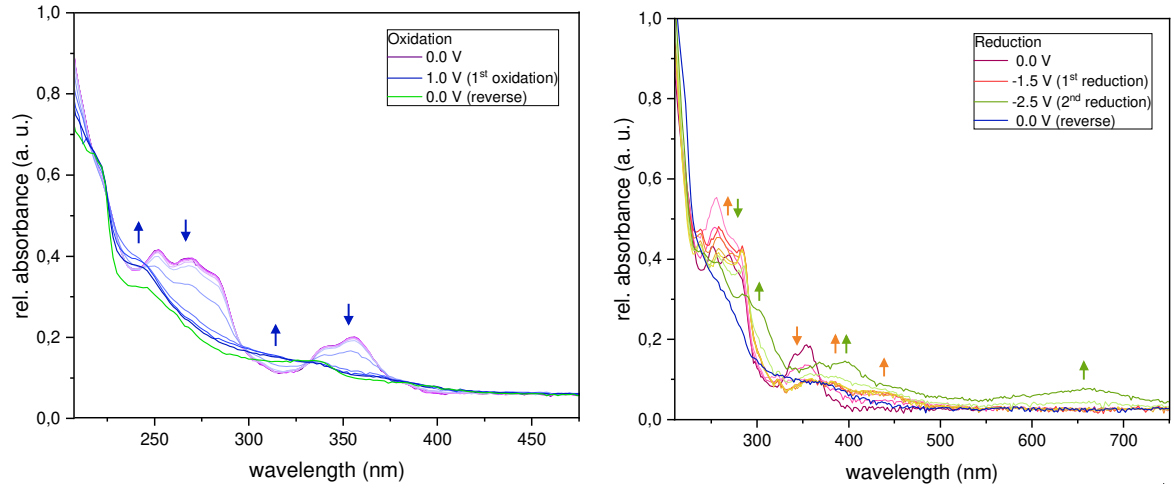

Fig. S40 UV-vis absorption spectra of [Pt(dpp)($SbPh_3$)] during anodic (left) and cathodic (right) electrolysis (spectroelectrochemistry) in 0.1 M *n*-Bu_4NPF_6 THF solution.

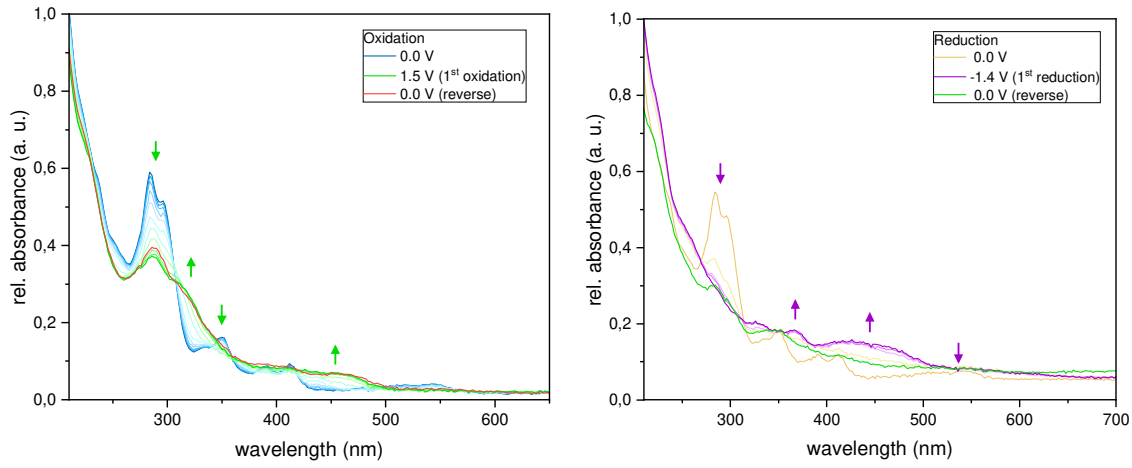

Fig. S41 UV-vis absorption spectra of [Pt(dba)($AsPh_3$)] during anodic (left) and cathodic (right) electrolysis (spectroelectrochemistry) in 0.1 M *n*-Bu_4NPF_6 THF solution.

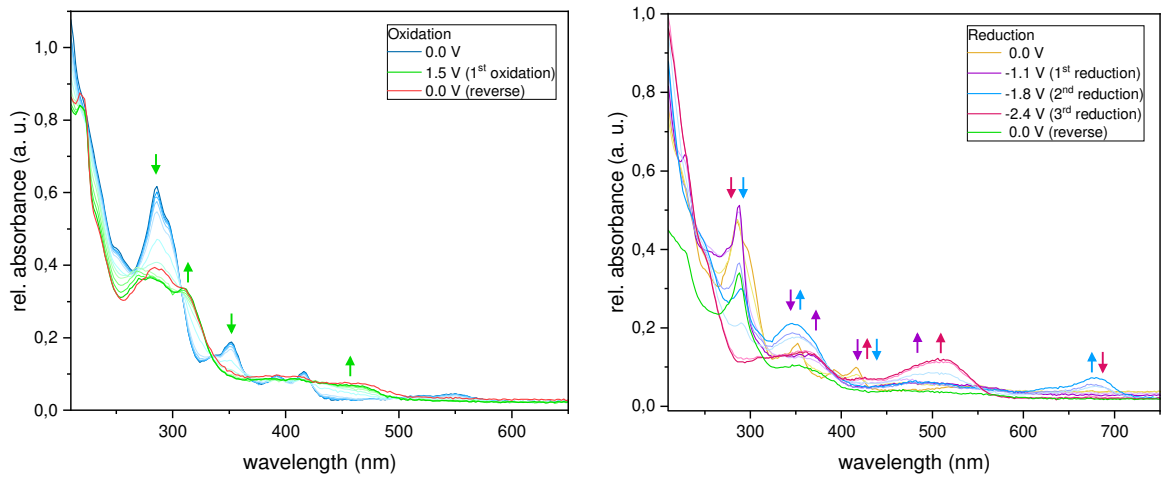

Fig. S42 UV-vis absorption spectra of [Pt(dba)($SbPh_3$)] during anodic (left) and cathodic (right) electrolysis (spectroelectrochemistry) in 0.1 M *n*-Bu_4NPF_6 THF solution.

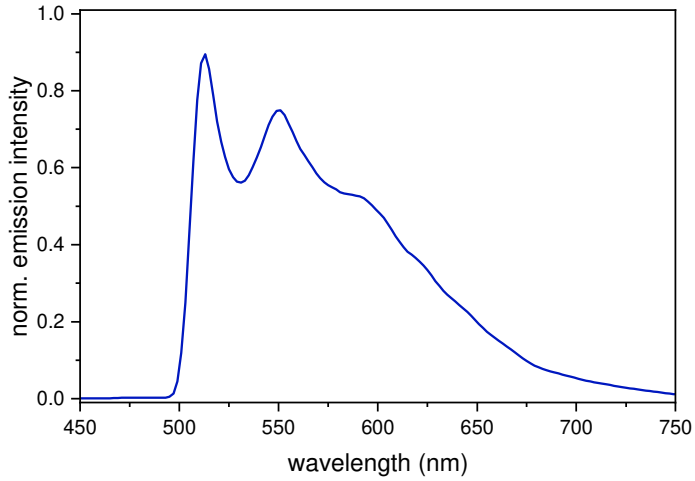

Fig. S43 Photoluminescence spectrum of [Pt(dpp)(PPh_3)] at 77 K in a frozen glassy MeOH/CH_2Cl_2 1:1 matrix, λ_{exc} = 350 nm.

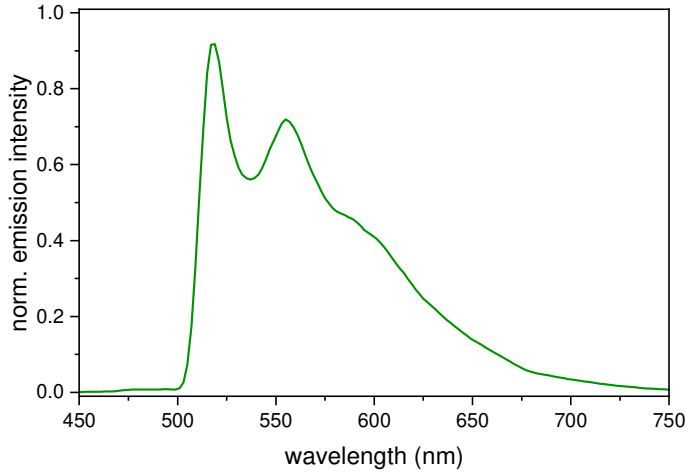

Fig. S44 Photoluminescence spectrum of [Pt(dpp)($AsPh_3$)] at 77 K in a frozen glassy MeOH/CH_2Cl_2 1:1 matrix, λ_{exc} = 350 nm.

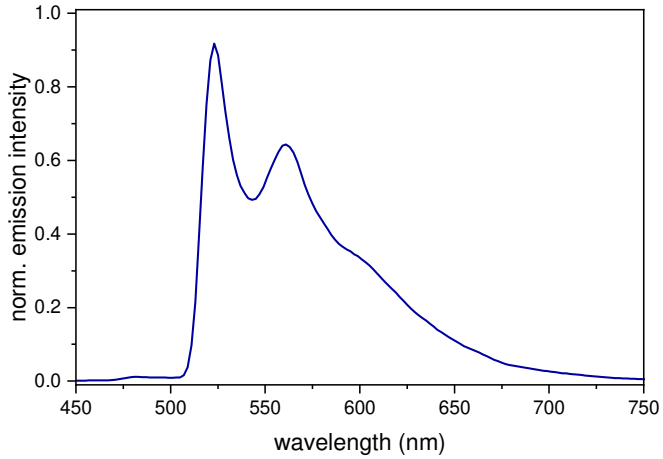

Fig. S45 Photoluminescence spectrum of [Pt(dpp)($SbPh_3$)] at 77 K in a frozen glassy MeOH/CH_2Cl_2 1:1 matrix, λ_{exc} = 350 nm.

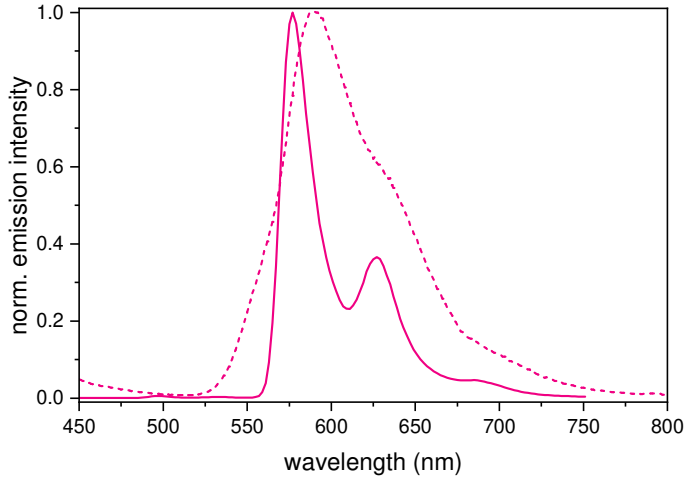

Fig. S46 Photoluminescence spectra of [Pt(dba)(PPh_3)] at 77 K in a frozen glassy MeOH/CH_2Cl_2 1:1 matrix (solid line) and in fluid CH_2Cl_2 solution at 298 K (dashed line) λ_{exc} = 350 nm.

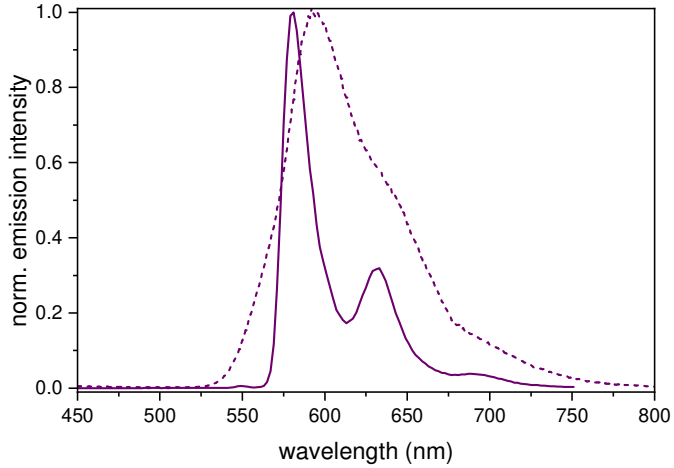

Fig. S47 Photoluminescence spectra of [Pt(dba)($AsPh_3$)] at 77 K in a frozen glassy MeOH/CH_2Cl_2 1:1 matrix (solid line) and in fluid CH_2Cl_2 solution at 298 K (dashed line), λ_{exc} = 350 nm.

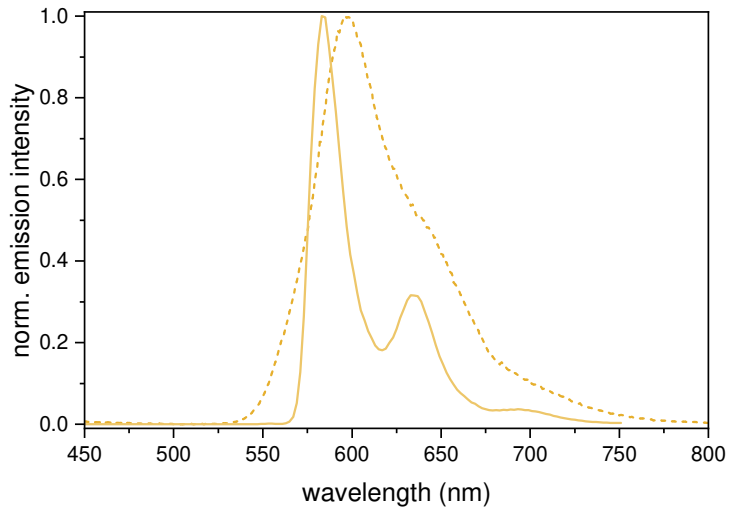

Fig. S48 Photoluminescence spectra of [Pt(dba)($SbPh_3$)] at 77 K in a frozen glassy MeOH/CH_2Cl_2 1:1 matrix (solid line) and in fluid CH_2Cl_2 solution at 298 K (dashed line), λ_{exc} = 350 nm.

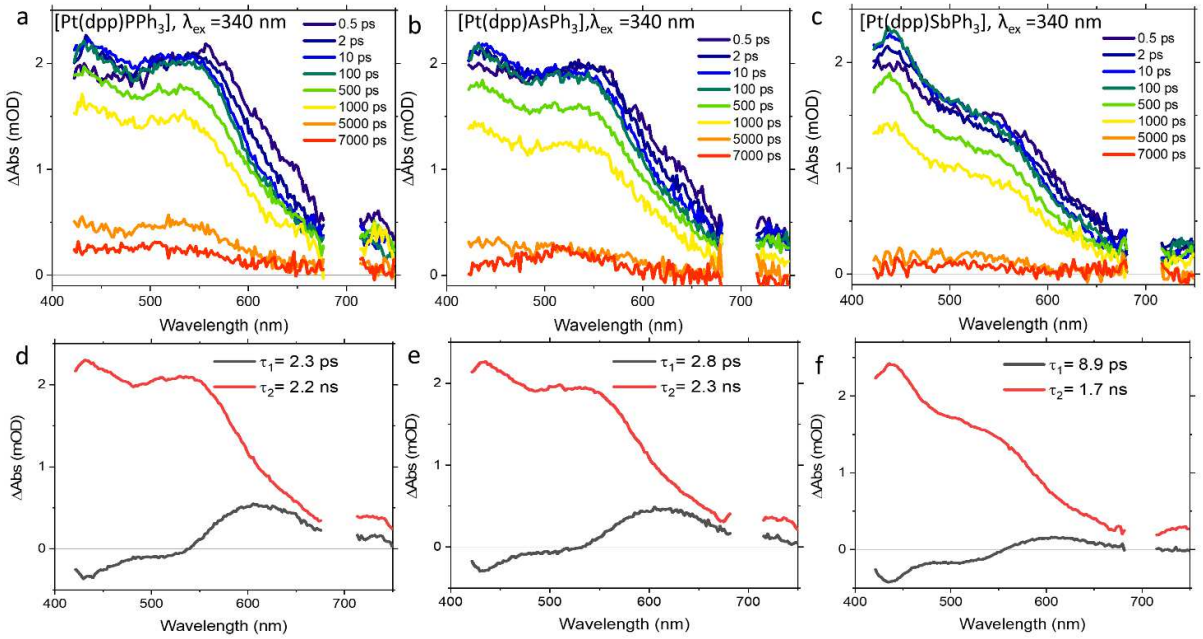

Fig. S49 Transient absorption spectra (TAS) at selected delay times (a-c) and decay associated spectra (d-f) for [Pt(dpp)(PPh_3)] (a and d), [Pt(dpp)($AsPh_3$)] (b and e) and [Pt(dpp)($SbPh_3$)] (c and f) upon excitation at 340 nm in THF.

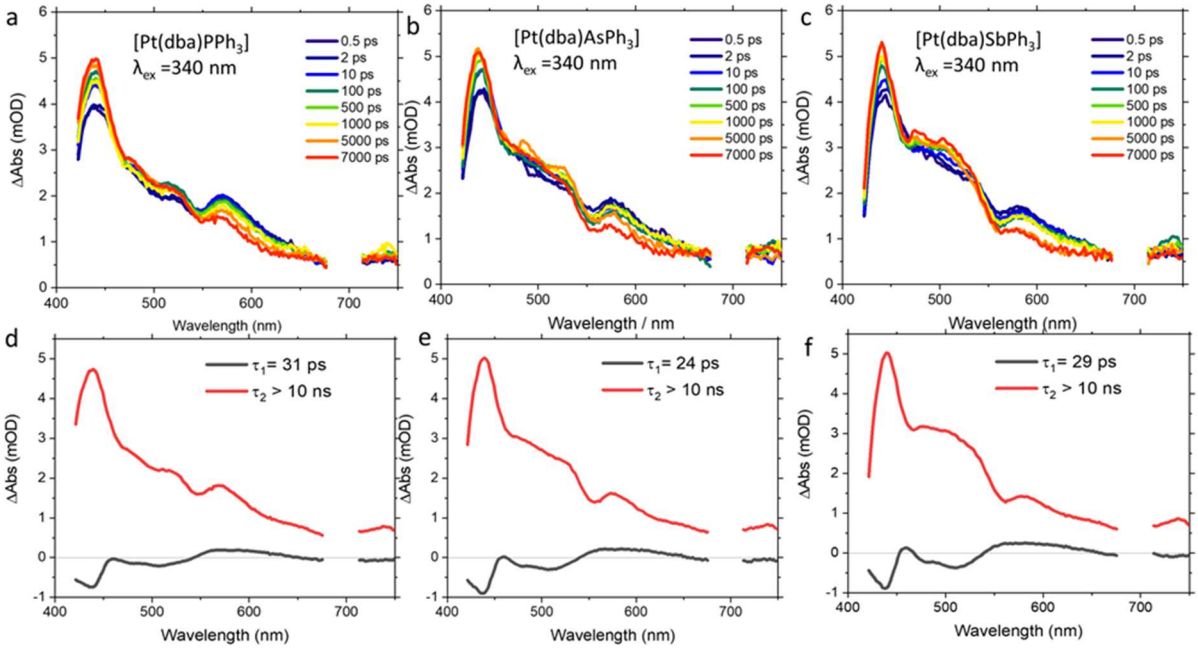

Fig. S50 TAS at selected delay times (a-c) and decay associated spectra (d-f) for [Pt(dba)(PPh3)] (a and d), [Pt(dba)(AsPh3)] (b and e) and [Pt(dba)(SbPh3)] (c and f) upon excitation at 340 nm in THF.

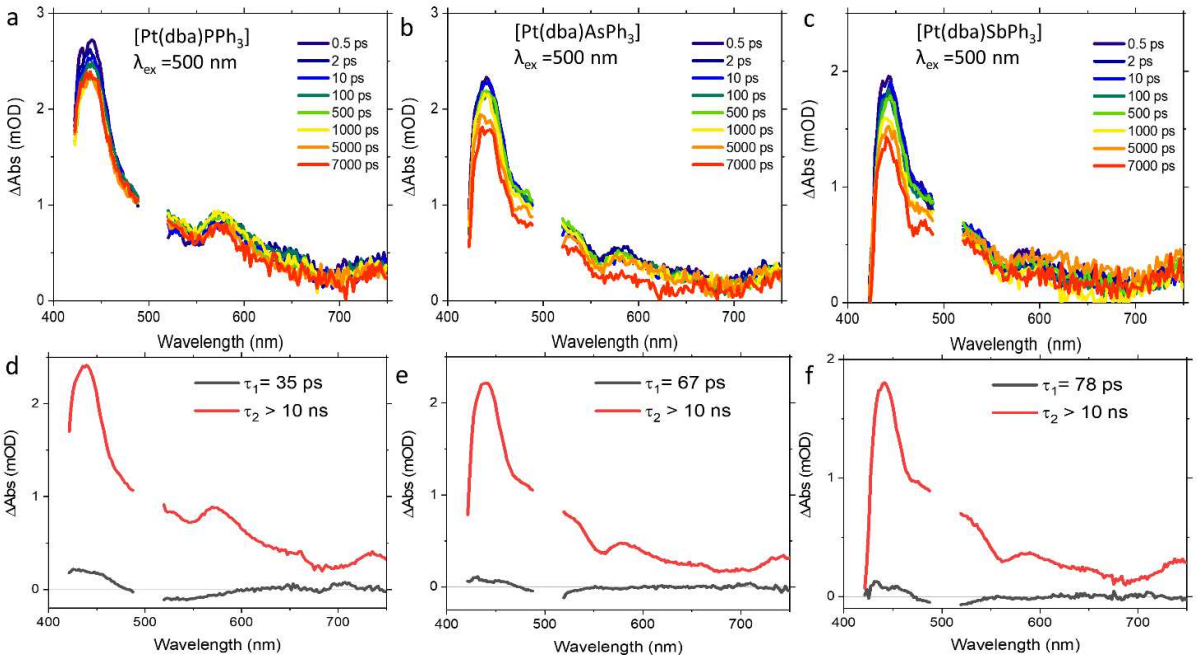

Fig. S51 TAS at selected delay times (a-c) and decay associated spectra (d-f) for [Pt(dba)(PPh3)] (a and d), [Pt(dba)(AsPh3)] (b and e) and [Pt(dba)(SbPh3)] (c and f) upon excitation at 500 nm in THF.

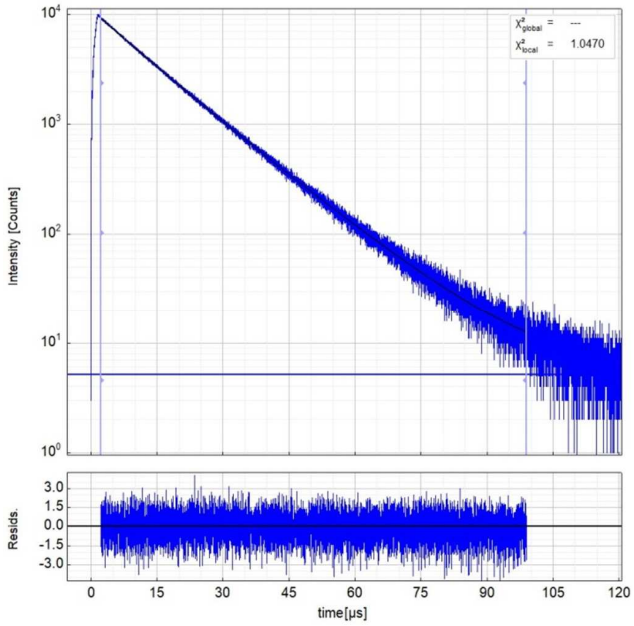

Parameter	Value	Δ	δ
A_1[kCnts/Chnl]	5.69	±0.54	9.4%
τ_1[ns]	14 490	±220	1.5%
I_1[kCnts]	10 310	±810	7.8%
A_{Rel1}[%]	61.7	±5.8	9.3%
I_{Rel1}[%]	70.3	±5.5	7.8%
A_2[kCnts/Chnl]	3.55	±0.53	15%
τ_2[ns]	9 860	±420	4.2%
I_2[kCnts]	4 370	±810	19%
A_{Rel2}[%]	38.4	±5.8	15%
I_{Rel2}[%]	29.8	±5.5	18%
$Bkgr_{Dec}$[kCnts]	0.0052	±0.0003	5.1%
τ_{AvInt}[ns]	13 107	±13	0.1%
τ_{AvAmp}[ns]	12 709	±13	0.1%

Fig. S52 Left: Raw (experimental) time-resolved photoluminescence decay of [Pt(dpp)(PPh_3)] in a frozen MeOH/CH_2Cl_2 1:1 glassy matrix at 77K including the residuals (λ_{ex} = 376 nm, λ_{em} = 510 nm). Right: Fitting parameters including pre-exponential factors and confidence limits.

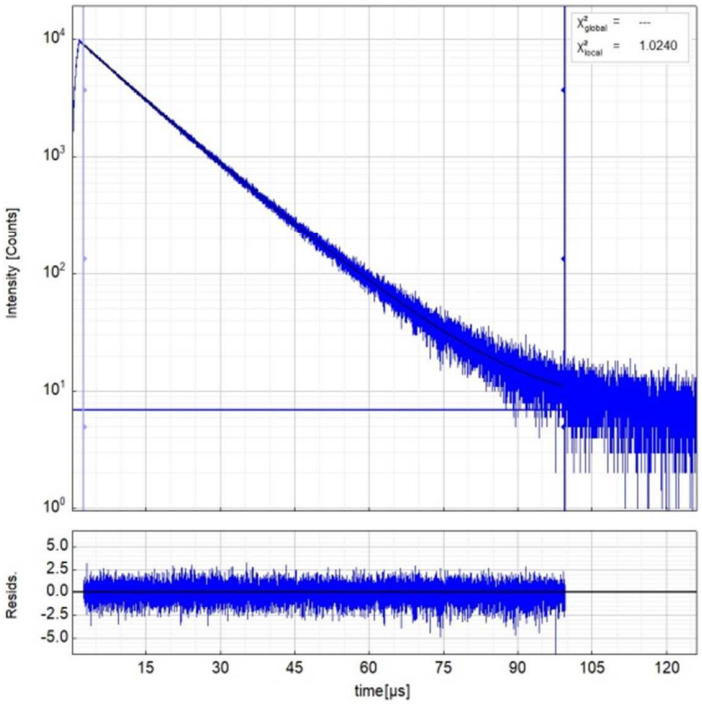

Parameter	Value	Δ	δ
A_1[kCnts/Chnl]	4.99	±0.69	14%
τ_1[ns]	13 570	±280	2.0%
I_1[kCnts]	8 460	±970	11%
A_{Rel1}[%]	55.9	±7.7	14%
I_{Rel1}[%]	64.3	±7.4	11%
A_2[kCnts/Chnl]	3.94	±0.69	17%
τ_2[ns]	9 570	±390	4.0%
I_2[kCnts]	4 700	±980	21%
A_{Rel2}[%]	44.2	±7.7	17%
I_{Rel2}[%]	35.8	±7.4	21%
$Bkgr_{Dec}$[kCnts]	0.0070	±0.0002	2.5%
τ_{AvInt}[ns]	12 133	±11	0.1%
τ_{AvAmp}[ns]	11 797.7	±8.3	0.1%

Fig. S53 Left: Raw (experimental) time-resolved photoluminescence decay of [Pt(dpp)($AsPh_3$)] in a frozen MeOH/CH_2Cl_2 1:1 glassy matrix at 77K including the residuals (λ_{ex} = 376 nm, λ_{em} = 515 nm). Right: Fitting parameters including pre-exponential factors and confidence limits.

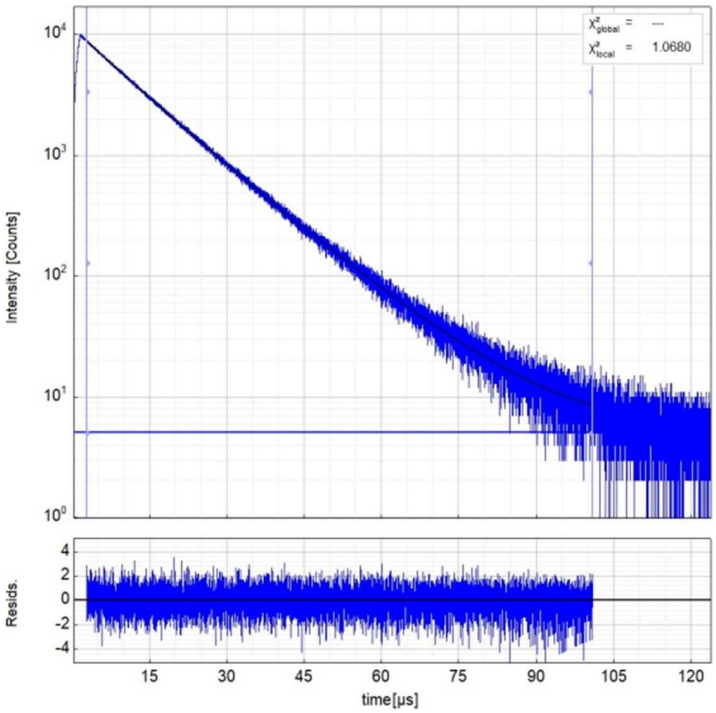

Parameter	Value	Δ	δ
A_1[kCnts/Chnl]	3.13	±0.31	9.7%
τ_1[ns]	14 210	±240	1.7%
I_1[kCnts]	5 550	±460	8.2%
A_{Rel1}[%]	35.9	±3.5	9.7%
I_{Rel1}[%]	44.0	±3.7	8.2%
A_2[kCnts/Chnl]	5.60	±0.30	5.3%
τ_2[ns]	10 130	±110	1.1%
I_2[kCnts]	7 080	±460	6.5%
A_{Rel2}[%]	64.2	±3.5	5.4%
I_{Rel2}[%]	56.1	±3.7	6.4%
$Bkgr_{Dec}$[kCnts]	0.0051	±0.0002	3.3%
τ_{AvInt}[ns]	11 916	±13	0.1%
τ_{AvAmp}[ns]	11 584.9	±7.0	0.1%

Fig. S54 Left: Raw (experimental) time-resolved photoluminescence decay of [Pt(dpp)($SbPh_3$)] in a frozen MeOH/CH_2Cl_2 1:1 glassy matrix at 77K including the residuals (λ_{ex} = 376 nm, λ_{em} = 515 nm). Right: Fitting parameters including pre-exponential factors and confidence limits.

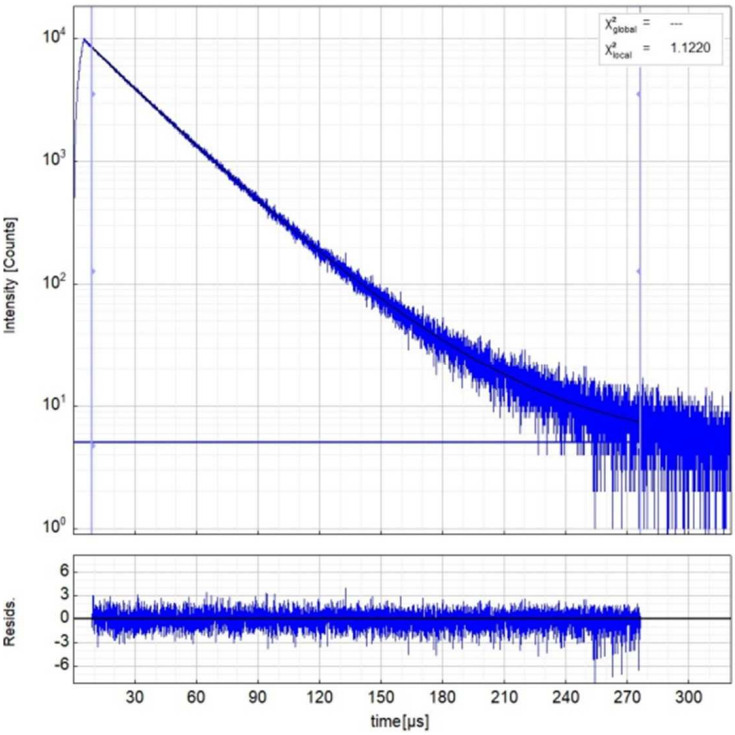

Parameter	Value	Δ	δ
A_1[kCnts/Chnl]	7.33	±0.40	5.3%
τ_1[ns]	25 620	±520	2.0%
I_1[kCnts]	5 870	±430	7.3%
A_{Rel1}[%]	86.8	±4.8	5.4%
I_{Rel1}[%]	79.7	±5.7	7.1%
A_2[kCnts/Chnl]	1.13	±0.41	36%
τ_2[ns]	42 900	±3 200	7.4%
I_2[kCnts]	1 510	±420	28%
A_{Rel2}[%]	13.3	±4.8	36%
I_{Rel2}[%]	20.4	±5.7	28%
$Bkgr_{Dec}$[kCnts]	0.0051	±0.0006	11%
τ_{AvInt}[ns]	29 128	±65	0.2%
τ_{AvAmp}[ns]	27 905	±64	0.2%

Fig. S55 Left: Raw (experimental) time-resolved photoluminescence decay of [Pt(dba)(PPh_3)] in a frozen MeOH/CH_2Cl_2 1:1 glassy matrix at 77K including the residuals (λ_{ex} = 376 nm, λ_{em} = 575 nm). Right: Fitting parameters including pre-exponential factors and confidence limits.

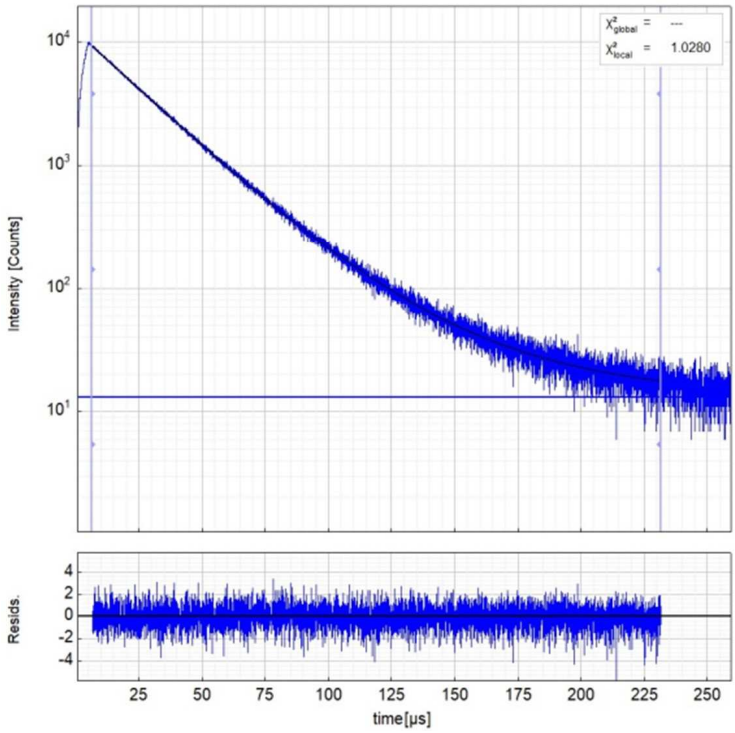

Parameter	Value	Δ	δ
A_1[kCnts/Chnl]	8.868	±0.090	1.0%
τ_1[ns]	22 590	±160	0.7%
I_1[kCnts]	6 260	±110	1.7%
A_{Rel1}[%]	95.9	±1.1	1.1%
I_{Rel1}[%]	91.3	±1.5	1.6%
A_2[kCnts/Chnl]	0.382	±0.099	26%
τ_2[ns]	50 400	±6 500	13%
I_2[kCnts]	600	±98	16%
A_{Rel2}[%]	4.2	±1.1	26%
I_{Rel2}[%]	8.8	±1.5	16%
$Bkgr_{Dec}$[kCnts]	0.0131	±0.0013	9.7%
τ_{AvInt}[ns]	25 010	±220	0.9%
τ_{AvAmp}[ns]	23 725	±65	0.3%

Fig. S56 Left: Raw (experimental) time-resolved photoluminescence decay of [Pt(dba)($AsPh_3$)] in a frozen MeOH/CH_2Cl_2 1:1 glassy matrix at 77K including the residuals (λ_{ex} = 376 nm, λ_{em} = 575 nm). Right: Fitting parameters including pre-exponential factors and confidence limits.

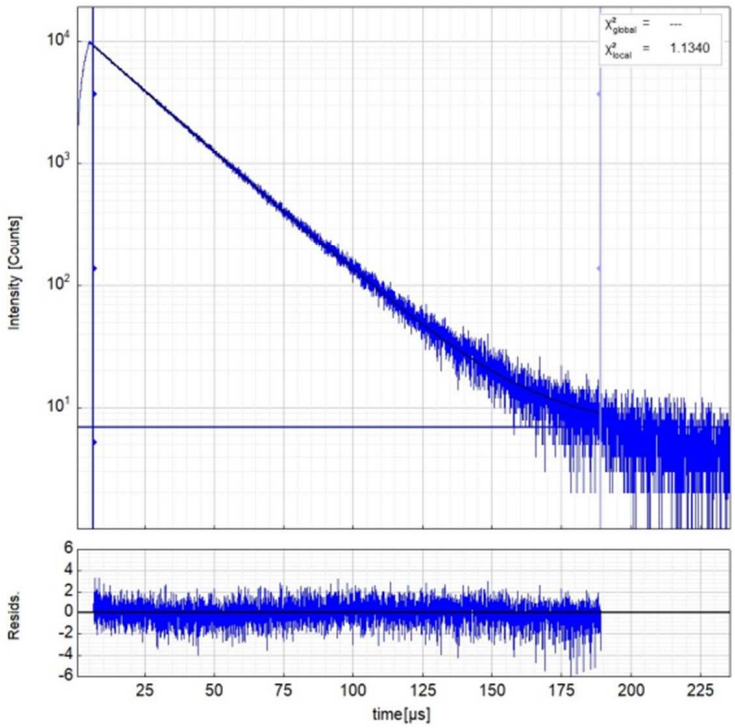

Parameter	Value	Δ	δ
A_1[kCnts/Chnl]	9.1815	±0.0100	0.1%
τ_1[ns]	21 912	±15	0.1%
I_1[kCnts]	6 286.9	±3.4	0.1%
A_{Rel1}[%]	100.0	---	---
I_{Rel1}[%]	100.0	---	---
$Bkgr_{Dec}$[kCnts]	0.0069	±0.0002	2.6%
τ_{AvInt}[ns]	21 912	±15	0.1%
τ_{AvAmp}[ns]	21 912	±15	0.1%

Fig. S57 Left: Raw (experimental) time-resolved photoluminescence decay of [Pt(dba)($SbPh_3$)] in a frozen MeOH/CH_2Cl_2 1:1 glassy matrix at 77K including the residuals (λ_{ex} = 376 nm, λ_{em} = 575 nm). Right: Fitting parameters including pre-exponential factors and confidence limits.

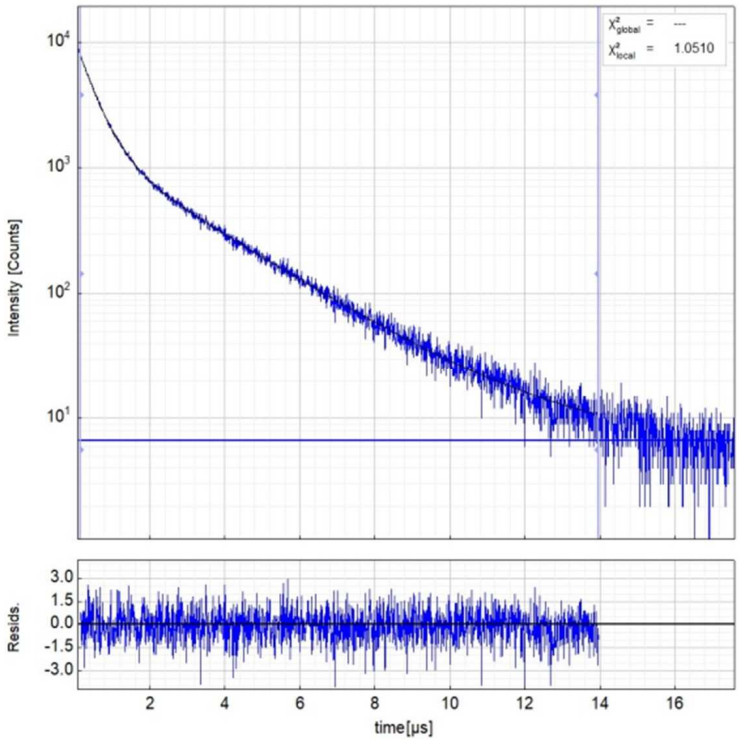

Parameter	Value	Δ	δ
A_1[kCnts/Chnl]	1.492	±0.015	0.9%
τ_1[ns]	2 352	±19	0.8%
I_1[kCnts]	438.4	±1.7	0.4%
A_{Rel1}[%]	19.1	±0.3	1.3%
I_{Rel1}[%]	55.2	±0.4	0.6%
A_2[kCnts/Chnl]	6.346	±0.040	0.6%
τ_2[ns]	449.2	±2.8	0.6%
I_2[kCnts]	356.3	±3.8	1.1%
A_{Rel2}[%]	81.0	±0.3	0.3%
I_{Rel2}[%]	44.9	±0.4	0.8%
$Bkgr_{Dec}$[kCnts]	0.0067	±0.0006	8.3%
τ_{AvInt}[ns]	1 498.6	±9.2	0.6%
τ_{AvAmp}[ns]	811.2	±4.3	0.5%

Fig. S58 Left: Raw (experimental) time-resolved photoluminescence decay of [Pt(dba)(PPh_3)] in fluid CH_2Cl_2 at 298 K including the residuals (λ_{ex} = 376 nm, λ_{em} = 600 nm). Right: Fitting parameters including pre-exponential factors and confidence limits.

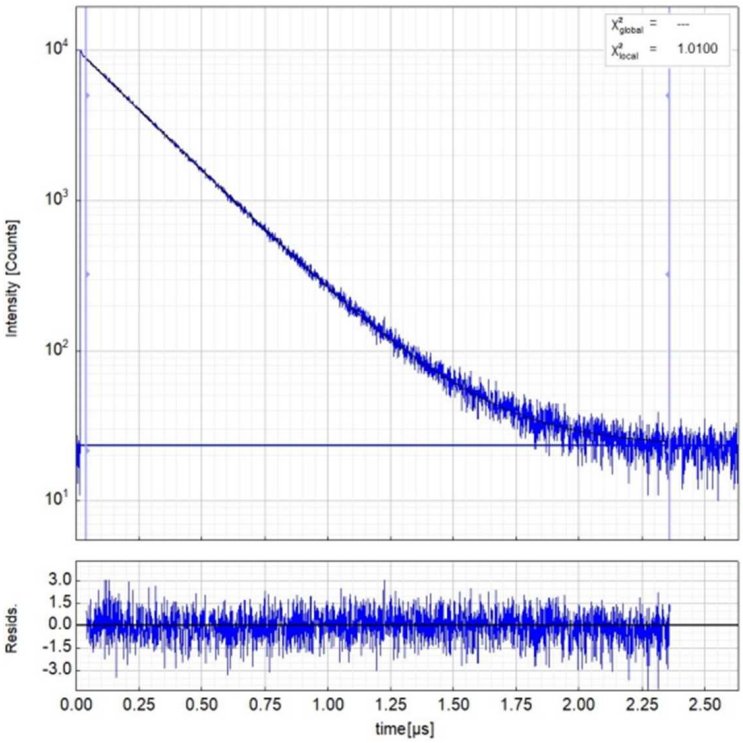

Parameter	Value	Δ	δ
A_1[kCnts/Chnl]	8.739	±0.013	0.1%
τ_1[ns]	268.40	±0.44	0.2%
I_1[kCnts]	2 345.5	±3.9	0.2%
A_{Rel1}[%]	100.0	---	---
I_{Rel1}[%]	100.0	---	---
$Bkgr_{Dec}$[kCnts]	0.0233	±0.0006	2.3%
τ_{AvInt}[ns]	268.40	±0.44	0.2%
τ_{AvAmp}[ns]	268.40	±0.44	0.2%

Fig. S59 Left: Raw (experimental) time-resolved photoluminescence decay of [Pt(dba)($AsPh_3$)] in fluid CH_2Cl_2 at 298 K including the residuals (λ_{ex} = 376 nm, λ_{em} = 600 nm). Right: Fitting parameters including pre-exponential factors and confidence limits.

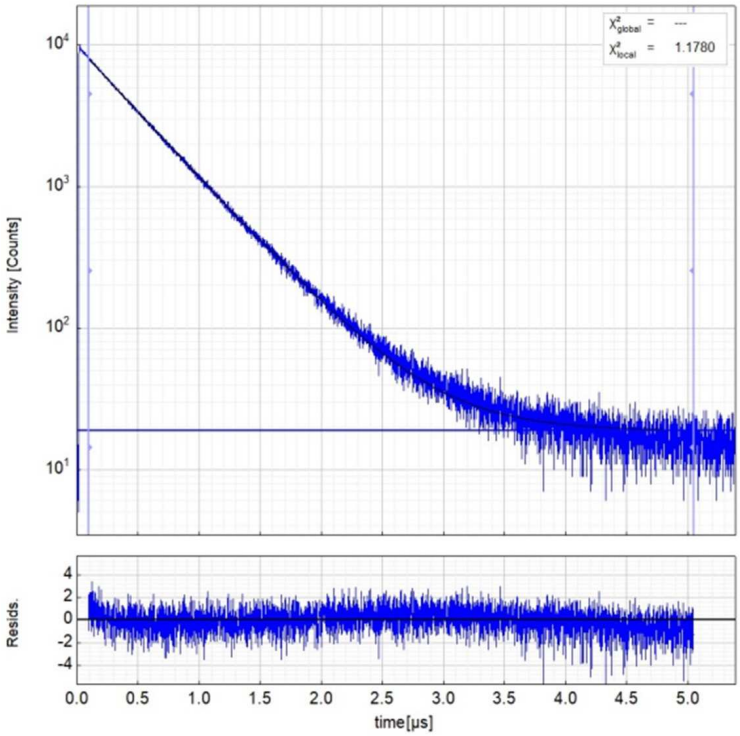

Parameter	Value	Δ	δ
A_1[kCnts/Chnl]	7.9869	±0.0097	0.1%
τ_1[ns]	469.23	±0.45	0.1%
I_1[kCnts]	3 747.7	±5.9	0.2%
A_{Rel1}[%]	100.0	---	---
I_{Rel1}[%]	100.0	---	---
$Bkgr_{Dec}$[kCnts]	0.0190	±0.0002	1.0%
τ_{AvInt}[ns]	469.23	±0.45	0.1%
τ_{AvAmp}[ns]	469.23	±0.45	0.1%

Fig. S60 Left: Raw (experimental) time-resolved photoluminescence decay of [Pt(dba)($SbPh_3$)] in fluid CH_2Cl_2 at 298 K including the residuals (λ_{ex} = 376 nm, λ_{em} = 600 nm). Right: Fitting parameters including pre-exponential factors and confidence limits.

Supporting Tables

Table S1 Selected structure solution and refinement data for crystal structures containing [Pt(C^N^C)($PnPh_3$)] (C^N^C = dpp, dba; Pn = As, Sb).

compound	[Pt(dpp)($AsPh_3$)]	[Pt(dba)($AsPh_3$)] ·Et_2O·$CHCl_3$ [a]	[Pt(dpp)($SbPh_3$)]	[Pt(dba)($SbPh_3$)]·0.5Et_2O
empirical formula	$C_{35}H_{26}AsNPt$	$C_{44}H_{37}AsCl_3NOPt$	$C_{35}H_{26}SbNPt$	$C_{82}H_{62}N_2OSb_2Pt_2$
formula weight (g/mol)	730.58	972.14	777.41	1725.10
temperature (K)	100(2)	109(2)	100(2)	100(2)
wavelength	Ag K_α	Mo K_α	Mo K_α	Mo K_α
crystal system	monoclinic	monoclinic	triclinic	triclinic
space group	$P2_1/c$	$C2/c$	$P\bar{1}$	$P\bar{1}$
cell parameters				
a (Å)	4.0056(6)	27.2312(16)	10.1552(6)	12.559(2)
b (Å)	9.5784(4)	10.5042(5)	15.5531(9)	13.453(2)
c (Å)	20.6896(9)	26.597(2)	17.832(1)	19.012(2)
α (°)	90	90	104.044(3)	99.710(4)
β (°)	96.219(2)	118.864(2)	97.175(3)	97.164(4)
γ (°)	90	90	90.067(2)	90.961(5)
V (Å^3)	2759.2(2)	6662.6(8)	2709.4(3)	3139.3(7)
Z	4	8	4	2
μ (mm^{-1})	3.41	5.35	6.18	5.35
crystal size (mm^3)	0.06 × 0.03 × 0.03	0.1 × 0.1 × 0.1	0.15 × 0.08 × 0.02	0.3 × 0.3 × 0.2
crystal colour/shape	yellow prism	red prism	orange prism	red prism
F(000)	1416	3412	1488	1668
2θ range (°)	1.9 – 22.0	3.0 – 30.5	2.0 – 30.2	2.0 – 28.3
index ranges				

$h_{min/max}$ $k_{min/max}$ $l_{min/max}$	–18 / 18 –12 / 12 –27 / 27	–38 / 38 –14 / 14 –37 / 37	–14 / 14 –21 / 21 –25 / 25	–16 / 16 –17 / 17 –25 / 25
reflections				
total independent	52922 6871	85756 10116	153953 15935	146817 15332
completeness	99.9%	99.9%	99.9%	99.9%
data / restraints / parameters	6871 / 0 / 343	10116 / 0 / 457	15935 / 0 / 667	15332 / 0 / 804
GooF on F^2	1.06	1.02	1.10	1.08
final R values				
R_1 ($I \geq 2\sigma(I)$/all data) wR_2 R_{int} R_σ	0.021/0.023 0.050 0.059 0.031	0.020/0.022 0.046 0.046 0.026	0.075/0.090 0.161 0.083 0.050	0.021/0.022 0.051 0.043 0.024
largest peak / hole ($e/Å^3$)	1.07 / –0.80	0.63 / –0.66	3.75 / –6.41	4.48[a] / –1.17
CCDC	2149899	2194357	2257280	2208288

[a] Due to the disordered solvent molecules Et_2O and $CHCl_3$ occupying special positions with respect to the cell symmetry, the refinement of these molecules was impaired and the corresponding H atoms could not be added to the model using AFIX in all cases. The H atoms missing in the structure solution were nonetheless included in the calculation of the empirical formula and formula weight. [b] This residual electron density is localised in direct proximity to the Et_2O molecule found in the structure and is attributed to its disorder which could not be explicitly refined.

Table S2 Selected structural data for [Pt(dpp)($PnPh_3$)] (Pn = P, As, Sb) from scXRD and DFT geometry optimisations of the S_0 states.[a]

	[Pt(dpp)(PPh_3)]		[Pt(dpp)($AsPh_3$)]		[Pt(dpp)($SbPh_3$)]	
	scXRD [a]	DFT	scXRD	DFT	scXRD [b]	DFT
distances (Å)						
Pt–N1	2.026(6)	2.042	2.008(2)	2.025	2.01(1)/2.03(1)	2.022
Pt–C7	2.065(6)	2.090	2.067(2)	2.083	2.08(1)/2.08(1)	2.081
Pt–C13	2.080(6)	2.090	2.066(2)	2.086	2.07(1)/2.06(1)	2.076
Pt–Pn	2.209(2)	2.234	2.321(1)	2.351	2.504(1)/2.491(1)	2.507
N1–C5	1.347(8)	1.358	1.347(3)	1.359	1.35(1)/1.36(1)	1.359
N1–C1	1.355(8)	1.357	1.353(3)	1.360	1.34(1)/1.35(2)	1.359
C5–C6	1.466(9)	1.468	1.471(4)	1.468	1.48(2)/1.47(2)	1.469
C1–C12	1.479(8)	1.468	1.474(4)	1.468	1.48(1)/1.48(2)	1.469
C6–C7	1.427(9)	1.434	1.431(4)	1.436	1.43(2)/1.44(1)	1.436
C12–C13	1.409(9)	1.436	1.423(4)	1.434	1.42(2)/1.42(2)	1.436
angles (°)						
C7–Pt–C13	159.8(2)	159.5	161.0(1)	160.5	160.6(4)/161.5(5)	161.0
Pn–Pt–N1	175.9(2)	174.9	175.8(1)	176.3	172.9(2)/170.2(2)	177.5
N1–Pt–C7	80.3(2)	79.9	80.7(1)	80.2	80.4(4)/81.0(4)	80.5
N1–Pt–C13	80.2(2)	79.7	80.9(1)	80.3	80.2(4)/80.5(4)	80.5
C7–Pt–Pn	97.6(2)	95.7	101.4(7)	103.3	97.4(3)/95.7(3)	97.0
C13–Pt–Pn	102.2(2)	104.8	97.3(1)	96.1	101.9(3)/102.6(3)	102.0
C–Pn–C averaged	104.1(2)	103.7	103.7(1)	102.7	98.3(2)/99.7(2)	101.2
C–Pn–Pt averaged	114.6(2)	114.8	114.9(1)	115.6	118.8(1)/118.1(1)	116.9
Sum of ∧ around Pt	360.3	360.1	360.3	359.9	359.9/360.2	360.0
dihedral angles (°)						
C7–Pt–Pn–C18	78.4(3)	56.6	97.3(1)	62.4	51.1(4)/66.8(5)	60.6
C13–Pt–Pn–C18	97.8(3)	121.6	79.4(1)	122.7	127.4(4)/115.6(6)	122.2
N1–Pt–Pn–C18	136.7(23)	85.6	143.2(8)	68.9	20(2)/136(2)	67.0
N1–C1–C12–C17	2.9(6)	2.7	11.1(2)	0.9	7(1)/4(1)	0.2

N1–C5–C6–C11	12.1(6)	2.6	2.3(2)	1.2	3(1)/0.51(1)	179.7

[a] scXRD data for [Pt(dpp)(PPh_3)] from ref.[1] [b] Data for two molecules in the unit cell.

Table S3 Selected structural data for [Pt(dba)($PnPh_3$)] (Pn = P, As, Sb) from scXRD and DFT geometry optimisations of the S_0 states.[a]

	[Pt(dba)(PPh_3)]		[Pt(dba)($AsPh_3$)]		[Pt(dba)($SbPh_3$)]	
	scXRD [a]	DFT	scXRD	DFT	scXRD [b]	DFT
distances (Å)						
Pt–N1	2.003(4)	2.030	1.996(2)	2.014	1.996(2)/1.994(2)	2.010
Pt–C1	2.099(5)	2.117	2.086(2)	2.115	2.110(3)/2.100(3)	2.107
Pt–C18	2.106(5)	2.122	2.101(2)	2.114	2.092(3)/2.098(3)	2.110
Pt–Pn	2.230(2)	2.232	2.335(1)	2.349	2.487(1)/2.493(1)	2.505
N1–C13	1.333(5)	1.340	1.334(3)	1.341	1.337(3)/1.332(3)	1.340
N1–C10	1.338(7)	1.339	1.335(3)	1.341	1.339(3)/1.340(3)	1.340
C13–C17	1.420(8)	1.426	1.428(4)	1.425	1.429(4)/1.425(3)	1.426
C10–C6	1.440(6)	1.426	1.421(3)	1.426	1.423(3)/1.425(4)	1.425
C17–C18	1.439(6)	1.440	1.448(3)	1.440	1.434(3)/1.432(3)	1.440
C6–C1	1.431(7)	1.438	1.432(3)	1.438	1.440(3)/1.435(4)	1.440
C7–C8	1.363(7)	1.373	1.356(3)	1.373	1.357(4)/1.365(4)	1.373
C14–C15	1.354(8)	1.373	1.361(4)	1.373	1.361(4)/1.359(4)	1.373
angles (°)						
C1–Pt–C18	158.6(2)	158.1	159.6(1)	158.1	159.5(1)/159.3(1)	159.4
Pn–Pt–N1	176.2(1)	175.8	176.5(1)	177.1	174.0(1)/177.3(1)	178.1
N1–Pt–C1	79.5(2)	79.2	80.1(1)	79.5	79.6(1)/79.8(1)	79.7
N1–Pt–C18	79.2(2)	79.0	79.6(1)	79.4	80.0(1)/79.5(1)	79.7
C1–Pt–Pn	96.8(1)	96.7	96.5(1)	97.7	102.9(1)/99.6(1)	102.2
C18–Pt–Pn	104.5(1)	105.1	103.8(1)	103.4	97.6(1)/101.1(1)	98.4
C–Pn–C averaged	104.3(1)	104.0	103.5(1)	103.0	102.5(1)/99.8(1)	101.5
C–Pn–Pt averaged	114.4(1)	114.5	114.9(1)	115.4	115.8(1)/118.2(1)	116.6
Sum of ∧ around Pt	360.0	360.0	360.0	360.0	360.1/360.0	360.0
dihedral angles (°)						
C1–Pt–Pn–C28	169.7(2)	174.0	69.9(1)	62.9	128.9(1)/170.0(1)	119.1
C18–Pt–Pn–C28	12.1(2)	4.4	108.6(1)	117.7	49.4(1)/10.9(1)	60.8
N1–Pt–Pn–C28	5.6(17)	8.9	73.5(9)	49.8	15.5(6)/112.0(1)	47.1
N1–C10–C6–C5	1.0(4)	1.1	1.7(2)	0.6	0.6(3)/1.2(2)	0.0
N1–C13–C17–C16	2.5(4)	1.3	0.2(2)	0.5	1.8(2)/0.8(2)	0.2
N1–C10–C9–C8	1.3(4)	0.5	0.5(2)	0.2	0.4(2)/0.4(2)	0.0
N1–C13–C12–C14	0.1(4)	0.6	0.3(2)	0.2	0.4(2)/1.5(2)	0.0
C14–C12–C11–C9	0.5(5)	0.9	0.1(2)	0.4	0.5(2)/0.9(3)	0.0

[a] Data for [Pt(dba)(PPh_3)] from ref.2. [b] Data for two molecules in the unit cell.

Table S4 Selected structural data for [Pt(C^N^C)($PnPh_3$)] (C^N^C = dpp, dba; Pn = P, As, Sb) from DFT geometry optimizations of the T_1 states.

	dpp				dba		
	P	As	Sb		P	As	Sb
distances (Å)				distances (Å)			
Pt–N1	2.033	2.021	2.025	Pt–N1	2.020	2.009	2.005
Pt–C7	2.060	2.054	2.051	Pt–C1	2.084	2.081	2.081
Pt–C13	2.054	2.050	2.049	Pt–C18	2.093	2.086	2.080
Pt–Pn	2.259	2.373	2.531	Pt–Pn	2.255	2.368	2.524
N1–C5	1.378	1.380	1.379	N1–C10	1.357	1.358	1.357
N1–C1	1.379	1.381	1.380	N1–C13	1.357	1.357	1.357
C5–C6	1.448	1.448	1.449	C13–C17	1.402	1.402	1.403
C1–C12	1.448	1.448	1.449	C10–C6	1.403	1.403	1.403
C6–C7	1.440	1.440	1.440	C17–C18	1.449	1.449	1.450

C12–C13	1.439	1.440	1.440	C6–C1	1.447	1.447	1.450
angles (°)				C7–C8	1.385	1.386	1.386
C7–Pt–C13	145.4	146.5	147.4	C14–C15	1.386	1.386	1.386
Pn–Pt–N1	174.2	174.5	174.4	angles (°)			
N1–Pt–C7	79.1	79.5	79.7	C1–Pt–C18	152.3	153.2	154.9
N1–Pt–C13	79.3	79.7	79.8	Pn–Pt–N1	176.6	177.1	178.1
C7–Pt–Pn	103.9	103.3	103.1	N1–Pt–C1	78.9	79.2	79.4
C13–Pt–Pn	100.3	99.8	99.7	N1–Pt–C18	78.6	79.0	79.3
C–Pn–C averaged	104.1	103.0	101.3	C1–Pt–Pn	98.3	98.2	98.7
C–Pn–Pt averaged	114.5	115.3	116.7	C18–Pt–Pn	104.6	103.8	102.6
Sum of ∧ around Pt	362.6	362.3	362.3	C–Pn–C averaged	104.1	103.1	101.4
dihedral angles (°)				C–Pn–Pt averaged	114.4	115.3	116.6
C8–C7–Pt–C13	121.3	122.2	124.3	Sum of ∧ around Pt	360.4	360.2	360.0
C7-Pt-C13-C14	123.0	123.1	124.4	dihedral angles (°)			
N1–C1–C12–C17	173.5	173.1	172.2	N1–C10–C6–C5	180.0	179.8	179.5
N1–C5–C6–C11	173.8	173.3	172.2	N1–C13–C17–C16	179.5	179.9	179.6
				N1–C10–C9–C8	178.7	178.6	178.6
				N1–C13–C12–C14	179.0	178.8	178.7
				C14–C12–C11–C9	175.6	174.7	175.5

Table S5 Selected structural data for [Pt(C^N^C)($BiPh_3$)] (C^N^C = dpp, dba) from DFT geometry optimisations of the S_0 state.

	[Pt(dpp)($BiPh_3$)]			[Pt(dba)($BiPh_3$)]
	free	constrained		constrained
distances (Å)			distances (Å)	
Pt–N1	2.065	2.004	Pt–N1	1.997
Pt–C7	2.080	2.076	Pt–C1	2.101
Pt–C13	2.102	2.065	Pt–C18	2.103
Pt–Bi	2.722	2.602	Pt–Bi	2.599
Pt–C_{Ph}	2.016	–		
N1–C5	1.356	1.360	N1–C13	1.342
N1–C1	1.354	1.362	N1–C10	1.343
C5–C6	1.471	1.469	C13–C17	1.425
C1–C12	1.474	1.467	C10–C6	1.424
C6–C7	1.434	1.435	C17–C18	1.439
C12–C13	1.435	1.436	C6–C1	1.438
			C7–C8	1.374
			C14–C15	1.373
angles (°)			angles (°)	
C7–Pt–C13	159.6	161.9	C1–Pt–C18	160.26
Bi–Pt–N1	87.6	175.8	Bi–Pt–N1	169.1
N1–Pt–C7	80.1	81.0	N1–Pt–C1	80.2
N1–Pt–C13	79.6	80.9	N1–Pt–C18	80.1
C7–Pt–Bi	101.1	98.3	C1–Pt–Bi	96.6
C13–Pt–Bi	79.7	99.8	C18–Pt–Bi	102.4
N1–Pt–C_{Ph}	175.7	–	C–Bi–C averaged	100.1
C7–Pt–C_{Ph}	98.5	–	C–Bi–Pt averaged	117.7
C18–Pt–C_{Ph}	101.6	–		–
Bi–Pt–C_{Ph}	96.7	–		–
C–Bi–C averaged	–	99.9		
C–Bi–Pt averaged	–	117.9		
Sum of ∧ around Pt	–	360.0	Sum of ∧ around Pt	359.3
dihedral angles (°)			dihedral angles (°)	
C7–Pt–Bi–C18	21.3	56.0	C1–Pt–Bi–C22	65.0

C13–Pt–Bi–C18	0.6	125.2	C18–Pt–Bi–C22	120.3
N1–Pt–Bi–C18	100.7	44.4	N1–Pt–Bi–C22	42.4
N1–C1–C12–C17	1.9	3.3	N1–C10–C6–C5	5.5
N1–C5–C6–C11	1.7	0.8	N1–C13–C17–C16	0.4
			N1–C10–C9–C8	5.5
			N1–C13–C12–C14	0.9
			C14–C12–C11–C9	3.1

Table S6 Electrochemical data for the ligands H_2dpp and H_2dba and the complexes [Pt(C^N^C)(PnPh$_3$)] (Pn = P, As, Sb).[a]

	Red3 E_p (V)	Red2 E_p (V)	Red1 $E_{1/2}$ (V)	Ox1 E_p (V)	ΔRed1-Red2	ΔRed1–Ox1
H_2dpp	–		–2.85	–		–
[Pt(dpp)(PPh$_3$)]	–	–2.96	–2.36	0.65	0.60	3.01
[Pt(dpp)(AsPh$_3$)]	–	–2.97	–2.36	0.56	0.61	2.92
[Pt(dpp)(SbPh$_3$)]	–3.36	–2.67	–2.26	0.61	0.41	2.87
H_2dba	–	–2.96	–2.31	–	0.65	–
[Pt(dba)(PPh$_3$)]	–3.26	–2.70	–2.00	0.72	0.70	2.72
[Pt(dba)(AsPh$_3$)]	–3.37	–2.68	–1.95	0.73	0.73	2.68
[Pt(dba)(SbPh$_3$)]	–3.28	–2.31[b]	–1.91	0.71	0.40	2.62

[a] Measured in 0.1 M nBu$_4$NPF$_6$ THF solution at a scan rate of 50 mV/s. Potentials E (V) referenced against the $FeCp_2/FeCp_2^+$ redox pair, accuracy of potentials: ± 0.003 V. $E_{1/2}$: half-wave potential for reversible processes, E_p: peak potential for irreversible processes. [b] Reversible, $E_{1/2}$ given.

Table S7 UV-vis absorption data of the ligand H_2dpp and the complexes [Pt(dpp)(PnPh$_3$)] (Pn = P, As, Sb).[a]

	λ_1 (ε)	λ_2 (ε)	λ_3 (ε)	λ_4 (ε)	λ_5 (ε)
H_2dpp	244 (27.2)	286 (11.1)	302 (10.8)	–	–
[Pt(dpp)(PPh$_3$)]	252 (38.4)	267 (34.3)	278 (34.8)	336 (13.8)	349 (15.7)
[Pt(dpp)(AsPh$_3$)]	252 (35.4)	265 (32.7)	281 (31.9)	339 (12.2)	352 (14.7)
[Pt(dpp)(SbPh$_3$)]	253 (36.7)	267 (34.9)	282 (31.7)	340 (12.9)	354 (15.5)

[a] Absorption maxima λ_n in nm in CH_2Cl_2, molar absorption coefficient in 10^3 M^{-1} cm^{-1}.

Table S8 UV-vis absorption data of the ligand H_2dba and the complexes [Pt(dba)(PnPh$_3$)] (Pn = P, As, Sb).[a]

	λ_1 (ε)	λ_2 (ε)	λ_3 (ε)	λ_4 (ε)	λ_5 (ε)	λ_6 (ε)	λ_7 (ε)	λ_8 (ε)
H_2dba	289 (8.2)	303 (7.6)	339 (1.6)	355 (1.1)	374 (1.3)	394 (1.8)	–	–
[Pt(dba)(PPh$_3$)]	286 (50.0)	296 (50.0)	333 (11.6)	348 (12.8)	387 (6.0)	409 (6.2)	499 (1.7)	533 (2.2)
[Pt(dba)(AsPh$_3$)]	285 (48.4)	296 (45.1)	333 (10.8)	354 (12.7)	390 (6.1)	412 (6.4)	505 (1.8)	539 (1.9)
[Pt(dba)(SbPh$_3$)]	286 (46.7)	296 (41.6)	335 (10.5)	351 (13.1)	392 (5.7)	416 (6.6)	511 (1.2)	546 (1.7)

[a] Absorption maxima λ_n in nm in CH_2Cl_2, molar absorption coefficient in 10^3 M^{-1} cm^{-1}.

References

1. A. Kergreis, R. M. Lord and S. J. Pike, Influence of ligand and nuclearity on the cytotoxicity of cyclometallated C^N^C platinum(II) complexes, *Chem.–Eur. J.*, 2020, **26**, 14938–14946. DOI: 10.1002/chem.202002517
2. J. N. Friedel, M. Krause, R. Jordan, I. Maisuls, D. Bruenink, D. Schwab, N. L. Doltsinis, C. A. Strassert and A. Klein, Triplet Emitting C^N^C Cyclometalated Dibenzo[c,h]Acridine Pt(II) Complexes, *Molecules*, 2022, **27**, 8054. DOI: 10.3390/molecules27228054
3. R. Siebert, D. Akimov, M. Schmitt, A. Winter, U.S. Schubert, B. Dietzek, J. Popp, Spectroscopic Investigation of the Ultrafast Photoinduced Dynamics in π-Conjugated Terpyridines, *ChemPhysChem*., 2009, **10**, 910-919, DOI: 10.1002/cphc.200800847
4. C. Müller, T. Pascher, A. Eriksson, P. Chabera, J. Uhlig, KiMoPack: A python Package for Kinetic Modeling of the Chemical Mechanism, *J. Phys. Chem. A*, 2022, **126**, 4087–4099, DOI: 10.1021/acs.jpca.2c00907
5. *APEX4—Software Suite for Crystallographic Programs*; Bruker AXS, Inc.: Madison, WI, USA, 2021.
6. G. M. Sheldrick, A short history of SHELX, *Acta Crystallogr. A - Found. Crystallograph.*, 2008, **64**, 112–122. DOI: 10.1107/S0108767307043930
7. G. M. Sheldrick, Crystal structure refinement with SHELXL, *Acta Crystallogr. C- Struct. Chem.*, 2015, **71**, 3–8. DOI: 10.1107/S2053229614024218
8. C. B. Hübschle, G. M. Sheldrick, B. Dittrich, ShelXle: a Qt graphical user interface for SHELXL, *J. Appl. Crystallogr.*, 2011, **44**, 1281–1284. DOI: 10.1107/S0021889811043202
9. F. Neese, F. Wennmohs, U. Becker und C. Riplinger, *J. Chem. Phys.*, 2020, **152**, 224108. DOI: 10.1063/5.0004608.
10. F. Neese, The ORCA quantum chemistry program package, *WIREs Comput Mol Sci.*, 2022, **12**, e1606. DOI: 10.1002/wcms.1606
11. F. Weigend and R. Ahlrichs, Balanced basis sets of split valence, triple zeta valence and quadruple zeta valence quality for H to Rn: Design and assessment of accuracy, *Phys. Chem. Chem. Phys.*, 2005, **7**, 3297. DOI: 10.1039/b508541a
12. A. D. Becke, Density-functional exchange-energy approximation with correct asymptotic behavior, *Phys. Rev. A*, 1988, **38**, 3098–3100. DOI: 10.1103/PhysRevA.38.3098
13. J. P. Perdew and W. Yue, Accurate and simple density functional for the electronic exchange energy: Generalized gradient approximation, *Phys. Rev. B*, 1986, **33**, 8800–8802. DOI: 10.1103/PhysRevB.33.8800
14. S. Grimme, J. Antony, S. Ehrlich and H. Krieg, A consistent and accurate ab initio parametrization of density functional dispersion correction (DFT-D) for the 94 elements H-Pu, *J. Chem. Phys.* 2010, **132**, 154104. DOI: 10.1063/1.3382344
15. S. Grimme, S. Ehrlich and L. Goerigk, Effect of the damping function in dispersion corrected density functional theory, *J. Comput. Chem.*, 2011, **2011**, 1456–1465. DOI: 10.1002/jcc.21759
16. V. Barone and M. Cossi, Effect of the damping function in dispersion corrected density functional theory, *J. Phys. Chem. A*, 1998, **102**, 1995–2001. DOI: 10.1021/jp9716997
17. M. Cossi, N. Rega, G. Scalmani and V. Barone, Energies, structures, and electronic properties of molecules in solution with the C-PCM solvation model, *J. Comput. Chem.*, 2003, **24**, 669–681. DOI: 10.1002/jcc.10189
18. J. Tao, J. P. Perdew, V. N. Stavoverov and G. E. Scuseria, Climbing the density functional ladder: Nonempirical meta–generalized gradient approximation designed for molecules and solids, *Phys. Rev. Lett.*, 2003, **91**, 146401. DOI: 10.1103/PhysRevLett.91.146401
19. Chemcraft – graphical software for visualization of quantum chemistry computations. https://www.chemcraftprog.com.
20. F. Plasser, TheoDORE: A toolbox for a detailed and automated analysis of electronic excited state computations, *J. Chem. Phys.*, 2020, **152**, 084108. DOI: 10.1063/1.5143076
21. E. van Lenthe, J. G. Snijders and E. J. Baerends, The zero-order regular approximation for relativistic effects: The effect of spin–orbit coupling in closed shell molecules, *J. Chem. Phys.*, 1996, **105**, 6505–6516. DOI: 10.1063/1.472460

22. D. A. Pantazis, X.-Y. Chen, C. R. Landis and F. Neese, All-Electron Scalar Relativistic Basis Sets for Third-Row Transition Metal Atoms, *J. Chem. Theory Comput.*, 2008, **4**, 908–919. DOI: 10.1021/ct800047t
23. J. D. Rolfes, F. Neese and D. A. Pantazis, All-electron scalar relativistic basis sets for the elements Rb–Xe, *J. Comput. Chem.*, 2020, **41**, 1842–1849. DOI: 10.1002/jcc.26355